AFRL-RD-PS-
TR-2019-0011

RECONFIGURABLE PLASMA METAMATERIAL FOR HIGH-POWER MICROWAVES (HPM)

Joshua L. Rovey, Matthew C. Paliwoda

30 January 2019

Final Report

AIR FORCE RESEARCH LABORATORY
Directed Energy Directorate
3550 Aberdeen Ave SE
AIR FORCE MATERIEL COMMAND
KIRTLAND AIR FORCE BASE, NM 87117-5776

NOTICE AND SIGNATURE PAGE

Using Government drawings, specifications, or other data included in this document for any purpose other than Government procurement does not in any way obligate the U.S. Government. The fact that the Government formulated or supplied the drawings, specifications, or other data does not license the holder or any other person or corporation; or convey any rights or permission to manufacture, use, or sell any patented invention that may relate to them.

This report was cleared for public release by AFMC Public Affairs Office and is available to the general public, including foreign nationals. Copies may be obtained from the Defense Technical Information Center (DTIC) (http://www.dtic.mil).

AFRL-RD-PS-TR-2019-0011 HAS BEEN REVIEWED AND IS APPROVED FOR PUBLICATION IN ACCORDANCE WITH ASSIGNED DISTRIBUTION STATEMENT.

//Robert Achenbach//

ROBERT ACHENBACH, DR-III
Work Unit Manager, AFRL/RDHP

//Stephen L. Langdon//

STEPHEN L. LANGDON, DR-III
Branch Chief, AFRL/RDHP

This report is published in the interest of scientific and technical information exchange, and its publication does not constitute the Government's approval or disapproval of its ideas or findings.

REPORT DOCUMENTATION PAGE

Form Approved
OMB No. 0704-0188

PLEASE DO NOT RETURN YOUR FORM TO THE ABOVE ORGANIZATION.

1. REPORT DATE *(DD-MM-YYYY)*	2. REPORT TYPE	3. DATES COVERED *(From - To)*
30-01-2019	Final Report	10-03-2017-30-12-2018

4. TITLE AND SUBTITLE
RECONFIGURABLE PLASMA METAMATERIAL FOR HIGH-POWER MICROWAVES (HPM)

5a. CONTRACT NUMBER
FA9451-17-1-0019

5b. GRANT NUMBER

5c. PROGRAM ELEMENT NUMBER

6. AUTHOR(S)
Joshua L. Rovey, Matthew C. Paliwoda

5d. PROJECT NUMBER

5e. TASK NUMBER

5f. WORK UNIT NUMBER
D0AU

7. PERFORMING ORGANIZATION NAME(S) AND ADDRESS(ES)
Missouri University of Science and Technology
300 West 12 St
Rolla, MO 65409-6506

8. PERFORMING ORGANIZATION REPORT NUMBER

9. SPONSORING/MONITORING AGENCY NAME(S) AND ADDRESS(ES)
Air Force Research Laboratory
3550 Aberdeen Avenue SE
Kirtland AFB, NM 87117-5776

10. SPONSOR/MONITOR'S ACRONYM(S)
AFRL/RDHP

11. SPONSOR/MONITOR'S REPORT NUMBER(S)
AFRL-RD-PS-TR-2019-0011

12. DISTRIBUTION/AVAILABILITY STATEMENT
Approved for public release; distribution is unlimited.
OPS-19-34978. AFMC-2019-0548

13. SUPPLEMENTARY NOTES
OPS-19-34978. AFMC-2019-0548

14. ABSTRACT
This research includes:
(1) a plane wave method simulation demonstrating viability of a photonic crystal formed from a dielectric barrier discharge (DBD) filaments with bandgaps between 5GHz and 300GHz
(2) finding that the presence and intensity of a single filament within an array of filaments is controllable by biasing a low voltage needle electrode with less than 7% of the driving voltage
(3) a 3D electrodynamic field simulation showing that increasing bias voltage causes changes in the transverse electric field structure, resulting in redistribution and build-up of surface charge at the needle
(4) establishment of a method for predicting filament pattern formation and reducing the necessary bias voltage

15. SUBJECT TERMS
dielectric barrier discharge (DBD), photonic crystal, controllable discharge array

16. SECURITY CLASSIFICATION OF:			17. LIMITATION OF ABSTRACT	18. NUMBER OF PAGES	19a. NAME OF RESPONSIBLE PERSON
a. REPORT	b. ABSTRACT	c. THIS PAGE			Robert Achenbach
unclassified	unclassified	unclassified	SA R	43	19b. TELEPHONE NUMBER *(Include area code)*

Reset

Table of Contents

List of Figures

1.0 SUMMARY

Filamentary volume dielectric barrier discharge (DBD) produces patterned plasma structures that are currently being explored for reconfigurable metamaterial applications. Our focus has been on developing controllable reconfigurability of these plasma DBD filaments. Major results of the research presented below are:

(1) a plane wave method simulation demonstrating viability of a photonic crystal formed from a DBD filaments with bandgaps between 5GHz (Gigahertz) and 300GHz
    a. Plasma frequency and filament radius can only control the normalized bandwidth of the bandgap.
    b. Lattice constant and background dielectric control the average frequency of the bandgap.
    c. Control of the average frequency provides the largest range of frequency space for the variable photonic crystal.
    d. Offsetting the plasma dielectric between adjacent filaments to artificially change the background dielectric could provide an alternative to controlling the position of the filament on a scale less than the smallest lattice constant.
(2) the presence and intensity of a single filament (within an array of filaments) is controllable by biasing a low voltage needle electrode by less than 7% of the driving voltage
(3) a 3D (three dimensional) electrodynamic field simulation shows that increasing needle bias voltage causes changes in the transverse electric field structure, resulting in redistribution and build-up of surface charge at the needle location
(4) criteria for filament extinguishment were determined, and are
    a. the applied longitudinal electric field profile along the needle lies below that of the adjacent mesh filament;
    b. the surface charge on the dielectric at the needle and adjacent mesh locations is equal; and
    c. the transverse electric field reverses direction and forces charge toward the needle location.
(5) a method for predicting filament pattern formation and reducing the necessary voltage bias has been determined and demonstrated
(6) Work has begun on an individually addressable 49 pin DBD plasma device designed to enable adjustable electric field/potential distribution and corresponding control over filament formation.

The following sections provide an introduction to the work, describe experimental results controlling a single filament within an array of filaments, electrostatic field modeling to determine controlling parameters of filament formation, and plane wave method simulations to predict the effect of filamentary DBD parameters on wave interactions. Additionally, in the future work section we outline current and planned activities to construct, test, and demonstrate an array of filamentary plasmas, as well as eventual experimental demonstration of reconfigurable/adjustable control of microwaves.

2.0 INTRODUCTION

Filamentary DBD plasma has been previously studied for application in the growing field of microwave "metamaterials" due to its electrically variable structure, electrically variable negative permittivity, and sub-microwave scale.[1] (Note: Metamaterials are artificial periodic composite structures that create permittivity and permeability not commonly found in nature, including negative values which can result in negative refraction of propagating electromagnetic waves.)[2] The collective electrical properties of a metamaterial are determined by the individual permittivity and permeability of the components as well as the structural arrangement of those components.[3–5] Plasma metamaterials have the potential to produce electrical material properties capable of being electrically tuned during operation over a large range of frequencies.

Plasma metamaterials are of specific interest for high power microwaves with application to directed energy weapons, plasma heating, radar, and high energy particle research.[6–8]

Plasma's potentially negative permittivity, defined by Equation (1),[9] makes it a prime candidate for metamaterial applications. The use of solid metamaterials results in gas breakdown,[10] material combustion,[11] and losses from failed components due to large electric fields between centimeter scale parts.[12] For plasma metamaterials, gas breakdown defines the microstructure which makes ionization a design consideration rather than a limitation

$$\varepsilon_{eff} = \left(1 - \frac{\omega_{\mathrm{pe}}^2}{\omega^2 - j\omega\nu_c}\right) \tag{1}$$

By adjusting the plasma frequency (ω_{pe}),defined by Equation (2),[9] the permittivity can be tuned between unity and negative values for the incident wave frequency (ω_{pe}). The electron density (n_{pe}), and hence the plasma filament permittivity (ε_{pe}), is effectively varied by the applied driving voltage,[1,13]

$$\omega_{pe} = \sqrt{\frac{n_e e^2}{\varepsilon_o m_e}} \tag{2}$$

The collision frequency, defined by Equation (3),[14] is dependent on the composition of the gas through the gas density (n_g), collisional cross-section (σ_{en}),[15] and drift velocity (u_e)[16] and gradually varies with the electron temperature. Combining Equations (1), (2), and (3), for the filamentary electron density at 10^{13} to 10^{15} cm^{-3} (Ref. [17]) and electron temperatures of 1 eV to 3 eV,[18–21] produces a negative permittivity for an incident wave at 110 Megahertz (MHz) (2.8 meters (m)) to 280 GHz (1.1 millimeters (mm))

$$\nu_c = n_g \sigma_{en} u_e \tag{3}$$

The malleable microstructure, which is the other attractive aspect for plasma metamaterials, is controlled by the voltage and frequency in a DBD.[13] DBD filaments are 0.1 mm diameter plasma columns across a gas gap between two dielectric covered electrodes.[22,23] A group of organized filaments, known as a plasma photonic crystal (PPC), induces an effective permittivity and permeability on transverse magnetic or transverse electric waves based on the size, position, and permittivity of individual filaments.[1,3,24]

Experimental and numerical tests have demonstrated PPC feasibility and potential. Sakai *et al*.[24–27] demonstrated band gaps in a PPC as well as a waveguide made of a single row of plasma columns. A non-DBD array of fixed capillary electrodes was used to form these plasma columns. Arrays of individual electrodes positioned behind a dielectric barrier have demonstrated filaments forming at, as well as between, the electrode positions with variations in the driving voltage and frequency.[28,29] Dong *et al*.[28,30–32]demonstrated a variety of self-organized DBD filaments for PPC applications, with the arrangement controlled by the driving voltage and frequency across two electrodes. In these cases, the filaments' position, size, and permittivity were either coupled through the applied frequency and voltage, or were non-variable. In order to demonstrate more exotic PPCs numerically predicted by Zhang *et al*.,[5,33,34] that are capable of negative refraction while remaining tunable, individual position control must be uncoupled from the filament permittivity. Uncoupling position control and filament permittivity is the focus of this work.

This work demonstrates an approach for achieving filament control by influencing the dynamics of the filament formation. Once a streamer is established across the gas gap, plasma acts as a highly conductive path for the electrons to transfer charge between the two dielectrics.[35,36] Surface charge then builds up on the dielectric in a Gaussian distribution until the applied electric field falls below the breakdown limit and extinguishes the filament.[37] Residual space and surface charge enhance the electric field during the reversed polarity of the driving voltage, causing a repeat discharge at the same location.[38] This work demonstrates the control of a single filament's light intensity, which is proportional to the electron density,[39] by influencing the charge distribution in the DBD, using a single electrode in an effective array of electrodes.

The intended application of filament control through charge distribution by individual electrodes is to form an array of electrodes behind a dielectric that controls each filament position and permittivity by manipulating the charge distribution over the entire dielectric. The relative voltage differences between individual needle electrodes would govern the position while the overall driving voltage would determine the permittivity of the filaments. This approach would uncouple the two main metamaterial parameters: filament permittivity and filament distribution. By only manipulating voltage differences at magnitudes necessary to induce charge distribution, rather than at magnitudes necessary for breakdown voltage, the electrode arrays could be more manageable for control circuits. The control method would remain purely electrical and tunable, extend the range of parameter variation, and allow the direct implementation of simulated PPC structures.

To demonstrate charge distribution control of a filament, Sections 3.1 and 3.2 describe the experimental setup and results from light intensity variation of a single filament within an array of filaments. A resistively biased needle controls the change in light intensity from the filament up until the filament no longer discharges. The surrounding array of filaments is formed by a mesh electrode to allow alternate current paths. Current, voltage, and light intensity data are presented as evidence that the voltage variations are magnitudes less than what would be necessary to reduce the cross gap voltage below the electric strength of air.

Then in Sections 3.3. and 4.1, we present electromagnetic field simulations within a DBD illustrating the effect of the biased voltage electrode on changes in the longitudinal and transverse electric field structure, as well as the change in free surface charge. Surface charge redistribution rather than the cross gap voltage difference is concluded as the mechanism through which the needle controls the filament light intensity and eventually extinguishes the filament. The results suggest a design methodology for achieving continuously tunable filament permittivity and position control.

3.0 METHODS, ASSUMPTIONS, AND PROCEDURES

3.1 Experimental Setup

The DBD investigated in this work consists of two parallel copper mesh electrodes, both covered with microscope slide glass. The driving signal mesh electrode allows for end-on photos of the filament position across the surface of the dielectric. The mesh and dielectric barrier that make up the driving electrode are of dimensions that create a uniform charge distribution over the discharging surface: 0.15 mm opening (#100 mesh size), 0.056 mm wire diameter, and 1.0 mm thick dielectric.[40,41] The grounded mesh electrode has an opening of 0.85 mm (#20 mesh size), a 0.40 mm diameter wire, and a dielectric barrier thickness of 0.1 mm. The larger mesh size and thinner dielectric barrier are sufficient to create an electric field on the surface of the grounded dielectric barrier, causing filaments to preferentially discharge at the mesh nodes. The vertical and horizontal weaves of the grounded electrode have an amplitude difference in their sinusoidal paths that keep the vertical weave 0.12 mm away from the glass surface at the mesh nodes where the wires cross. The peak to peak sinusoidal amplitude of the horizontal wire weave is 0.92 mm and that of the vertical wire weave is 0.68 mm.

The DBD mount, an acrylonitrile butadiene styrene (ABS) plastic stand, has acme screws on the side to permit fine tuning of the gap width. The effective discharging surface area of the DBD is 22 mm X 22 mm. Adhesive gel on the edge of the mesh prevents charge from making a direct path to the mesh electrodes around the edge of the dielectric. This ensures that the current travels through the dielectric. When the DBD operates at 6.5 kV (kilovolt) and 7.5 kV, the air gap is 1.0 mm wide, and when it operates at 9.0 kV, the air gap is 1.5 mm wide. For all conditions, the frequency is 3.2 kHz (kilohertz).

An independently biased needle controls the light intensity of a plasma filament within the DBD. A magnetic wire with flattened tip mounted flush to the back surface of the grounded dielectric barrier forms the needle. The wire (diameter 0.57 mm) with an added Kapton insulation layer (0.14 mm thickness, $\varepsilon = 3.5$) fits through the mesh, so that the only electrical connections between the two are through the dielectric or their respective biasing connections to ground. Resistors connect the needle to ground, causing the needle to have a non-zero, or self-biasing, voltage. Changing resistance adjusts the self-biasing voltage of the needle.

Figure 1 shows the electrical and instrumental schematic of the experimental setup. The driving voltage signal is created by a Rigol DG-1022 Function Generator. The power for the discharge is supplied by a Crown Macro-Tech 1202 Audio Amplifier. A Corona Magnetics 5525–2 Transformer with a turn ratio of 1:357 increases the signal to the driving voltage. A North Star PVM-5 High Voltage Probe, with a 1:1000 ratio, monitors the voltage supplied to the DBD. A 1:1 Pearson Current Probe, Model 114, monitors the total current through the system. A 1:10 Tektronix P2221 passive voltage probe reads the voltage across a 200 kΩ (kilo ohm) resistor

in series with the larger biasing resistor that controls the voltage at the needle. An Agilent Infinium 500 MHz 1GSa/s Model #54815A oscilloscope records both the Pearson and the North Star probe signals. A Canon EOS Rebel XL records the time-averaged discharge of the filament position and light intensity at an exposure time of 125 ms (millisecond).

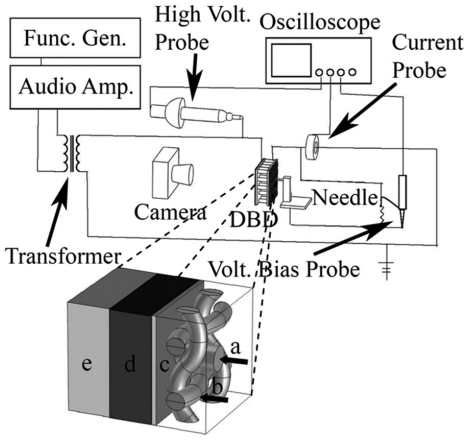

Figure. 1. Diagram of the experimental setup w ith the solid model inset showing the needle location with respect to mesh nodes. The solid model shows the DBD layers consisting of (a) needle electrode, (b) grounded wire mesh and mesh node (where weaves cross), (c) 0.12 mm thick glass dielectric, (d) 1.0 mm air gap, and (e) 1.0 mm thick glass dielectric.

3.2 Experimental Results

3.2.1 Filament photographs

Photographs of the DBD filaments for different self-biasing needle resistances are shown in Figure 2. These data are for the 6.5 kV driving voltage. The light from each discharge cycle was collected over the total camera exposure time of 125 ms creating a time integration of 875 filament discharges per data point. Only the lowest quarter of the digital photos' histograms were populated, signifying that none of the photocells in the camera were over saturated. The regular pattern of dots is made up of individual DBD plasma filaments forming where the grounded wire mesh electrode contacts the dielectric. The filaments form at alternating mesh nodes due to the height difference between the vertical and horizontal weaves. For resistances below 10 MΩ (Mega ohm), a filament clearly forms in between the wire mesh nodes at the needle location. As the self-biasing resistance of the needle increases, the filament light intensity decreases. It is clear from these photographs that the independent needle can control both the presence and intensity of the new filament. Resistance below 200 kΩ was investigated with a 1 kΩ resistor; however, prominent current spikes reduced the reliability of the measurements. Resistances above 30 MΩ were not investigated because the data showed that further increases had no effect on the discharge of the filament.

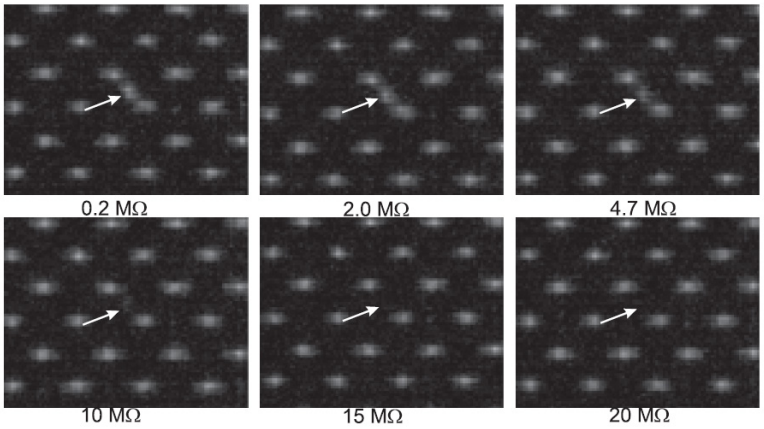

Figure 2. Photographs of the filament at the needle within the mesh filament array. End on view of the dielectric surface with the DBD driving voltage operating at 6.5 kV. The resistances between the needle and ground are given. The arrow indicates the needle filament position.

The needle filament position is always in the same location, to within ~3%. The needle filament position is calculated based on the light intensity from the photos and compared with the diagonal line between the two adjacent wire mesh filaments. Along the diagonal, the needle filament position varies by 3% (~0.05 mm) from the midpoint between the adjacent filaments. Perpendicular to the diagonal, the needle filament position varies by less than 1% (~0.018 mm). These measures provide a level of confidence to this method.

A photographic analysis is presented in order to obtain a better measure of the light intensity change at the needle-controlled filament. The average numerical value of the photograph pixels at the needle-controlled filament location is compared with the average pixel value at a reference mesh filament located three filaments away from the needle. An 8 × 8 pixel square section of the photograph, fitting the size of the filament, was selected using Photoshop software. The average background pixel value, taken from the midpoint between two mesh filaments, was subtracted from the filament pixel value. A 15 × 15 pixel square section was used to select the region without any discharge. In this way, the intensity of the needle-controlled filament is compared with a mesh filament. Figure 3 shows the results as the ratio of the needle filament to the mesh filament for 6.5 kV, 7.5 kV, and 9.0 kV. The error bars were created by measuring the light intensity of the same ten mesh filaments surrounding the needle location and its immediately adjacent mesh filaments, taking the standard deviation between photos, averaging that value, and creating a ratio with respect to the reference filament intensity.

The needle-controlled filament has a distinct on- and off-state. For resistances at 15 MΩ and above, the ratio of the needle-filament to the mesh-filament goes to zero, signifying that the light intensity is the same as a non-discharging region. At this point, the ratio of the needle filament to the mesh is zero since the background is subtracted from the needle value. Assuming that there is no discharge in the mesh gap, this ratio signifies that no discharge occurs at the needle's position. The measured luminosity in the regions without filaments is due to ambient light and the inherent noise level of the camera. As the resistance decreases, the needle-filament turns on and

becomes more intense. At the lowest resistance tested (200 kΩ), the needle-filament has an intensity around 100% of the mesh-filament intensity for 6.5 kV, 7.5 kV, and 9.0 kV correlating to a fully on filament.

Although the intensity values of all three driving voltages are within the significant error limits for 200 kΩ, 2 MΩ, and most significantly the turn-off resistance 15 MΩ, the 7.5 kV condition deviates by 160% at 10 MΩ and 30% at 4.7 MΩ, from the 6.5 kV condition. The wire of the mesh that curves away from the back of the dielectric can support additional charge on the dielectric surface within the gas gap contributing to the filament characteristic surface charge.17 Visually, discharge activity in the photos of the 7.5 kV condition covers an increased surface area along the wire mesh in comparison to the 6.5 kV and 9.0 kV photos. The additional charge, for 4.7 MΩ and 10 MΩ, could offset the charge siphoned from the needle filament to the adjacent filaments. The gas gap for the 9.0 kV condition is 1.5 mm instead of 1.0 mm, which prevents over saturation on the dielectric surface along the wire. However, there is a dynamic that overcomes this additional charge at 15 MΩ, since all filaments have significantly the same intensity for this resistance.

Finally, Figure 3 shows that the intensity ratio is almost the same for all applied voltages, within the error bars except for the 10 MΩ case. This is to be expected when one considers that filament light intensity is correlated with the needle and driving voltages (electric fields), and that the needle voltage changes correspondingly with the driving voltage. The needle voltage is shown in Figure 4. For the same needle bias resistance, the needle voltage increases corresponding with the increase in driving voltage. For example when the driving voltage increases 15% from 6.5 to 7.5 kV, at 5 MΩ the needle voltage increases 15% from 209 to 238 V (Volt), at 2 MΩ the increase is 15% from 97 to 113 V. Light intensity of plasma filament formation and propagation in air is proportional to the ionization activity, which is related to the bias voltage and corresponding electric field.42–44 As driving voltage increases, needle voltage increases proportionally, and filament intensity increases by about the same amount at both the needle and wire mesh locations such that the ratio of filament intensity is only weakly dependent on the driving voltage, as shown in Figure 3. More details about the movement of charge across the air gap, the build-up of charge on the dielectric surfaces, and the filament formation process are presented in Sections 4.1 and 4.2.

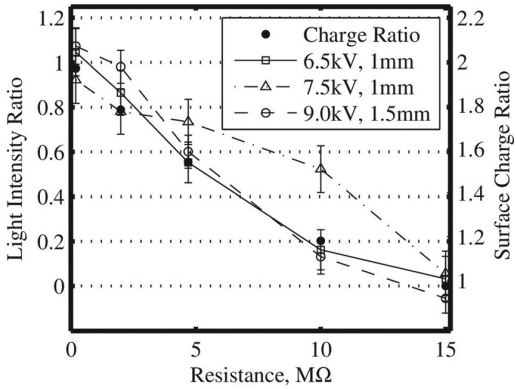

Figure 3. Measured light intensity ratio between the needle and mesh filaments as a function of resistance at 6.5 kV, 7.5 kV, and 9.0 kV. Simulated total surface charge ratio between the needle and mesh locations as a function of needle bias resistance (Discussed in Section V.D). The measured light intensity ratio is directly proportional to the simulated surface charge ratio. (Lines are used for clarity.)

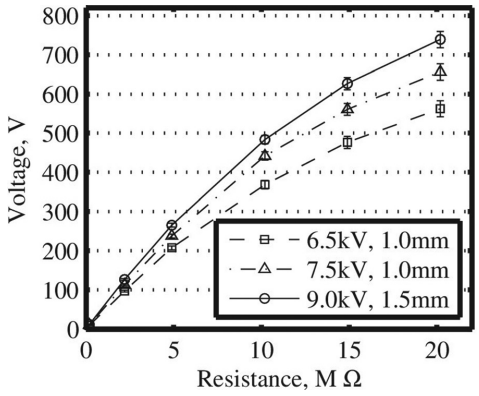

Figure 4. Voltage as a function of resistance at 6.5, 7.5, and 9.5 kV. Changes to the needle's voltage due to changing resistors between the needle and ground.

3.2.2 Needle voltage and current

Adjusting the needle self-biasing resistance affects the needle voltage and current. The voltage at the needle does not rise linearly, as it curves with increased resistance, as shown in Figure 4. Although the voltage looks like it might approach a limit, the point of interest where the needle filament ceases to discharge is met before any definitive evidence of a limit develops from increased resistance. The voltage for the turn-off of the filament at the needle is 476 V, 560 V, and 626 V respective to the driving voltages 6.5 kV, 7.5 kV, and 9.0 kV. All of these values correspond to 7% of the driving voltage. The difference between the observed on- and off-state, 10 MΩ to 15 MΩ, is 108 V, 119 V, and 143 V respective to the driving voltages 6.5 kV, 7.5 kV, and 9.0 kV.

The external voltage suppression caused by the biasing resistor at the 7.5 kV driving voltage is not large enough to bring the voltage difference across the air gap to the voltage difference of the 6.5 kV driving discharge. This implies that the intensity variation is not purely a result of reducing the voltage difference across the air gap, but rather preferential discharge at peak charge locations on the dielectric. In other words, more complex surface charge dynamics are responsible for these results rather than just the magnitude of the voltage difference across the air gap located at the needle.

The current through the needle is shown in Figure 5. The current decreases linearly with the resistance. Although light intensity shows that there is no longer a filament forming at the needle, current continues to pass through the needle. The current drop between 200 kΩ and 15 MΩ remains the same for all driving voltages. The amperage offset suggests a uniform current that passes through all fully formed filaments. Since the current drop is only about a 27% decrease, the amount of charge forming over the needle on the dielectric must also remain of the same magnitude. With the voltage difference across the gap changing by only 7% and a current drop of only 27%, the electric field across the DBD must be displaced by an alternate charge movement mechanism in order to prevent breakdown of the air and formation of a plasma filament.

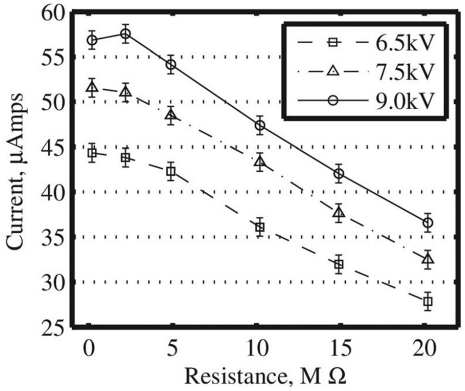

Figure 5. Current as a function of resistance at 6.5, 7.5, and 9.5 kV. Changes to needle's current due to changing resistors between the needle and ground.

3.3 ELECTROSTATIC DBD FIELD SIMULATION SETUP

The simulations presented below were designed to replicate the experimental conditions. Our goal here is to study changes in the electric field within the DBD gap due to the varied needle potential, and correlate those changes with variations in the needle filament light intensity and the corresponding turn-off condition. The commercial software Computer Simulations Technologies (CST) Electromagnetic Studios[45] was used to simulate the electric fields within the DBD. This finite element software solves a range of electromagnetic problems. The solver selected for this simulation was the Low Frequency (LF) Domain solver with the electroquasistatic equations (Equations (4)–(6)).[46] The peak voltage boundary conditions are substituted for the electric field using Equation (7)[47] and the spatially discretized equations are solved for the electric field and current densities. These equations ignore the magnetic induction and depend on the source at a single instant in time without regard to the fields at the previous instant in time. In this case, an electrostatic description of the field is obtained for the maximum field values. The solver selection is valid since the problem is dominated by the electric field if the frequency was brought to a static state and since the ratio of the characteristic size to the applied field wavelength is much less than one ($10^{-8} << 1$).

$$\nabla \cdot E = \frac{\rho}{\varepsilon_o} \tag{4}$$

$$\nabla \times E = 0 \tag{5}$$

$$\nabla \cdot J + i\omega\rho = 0 \tag{6}$$

$$E = -\nabla\phi \tag{7}$$

Although the simulation assumes (1) no free charge movement within the air gap, and (2) that the filament formation process displaces the field during discharge, the electrostatic results provide an understanding of the initially applied field that must be displaced during discharge. In other words, the electrostatic results elucidate the vacuum fields that are present as the filament forms.

These vacuum fields guide the electron motion and subsequent energy gain that leads to the gas breakdown and filament formation. Since the formation of the filament occurs over ~200 ns (nanosecond),[48] the applied electric field, with a 312.5 μs (microsecond) period (3.2 kHz), was considered constant during the filament formation process. In Section III, we correlate changes in the simulated electric field (due to different needle bias) with changes in the experimentally measured filament light intensity. In the context of charged particle movement, the field simulations can explain the observed filament intensity variation.

The 3D model was created using the CST in-house computer-aided design (CAD) software. The wire mesh of the model, shown in Figure 6, replicates an inherent height difference between lateral and horizontal weaves. When placed against the surface of the dielectric, the wire closest to the surface creates the lowest potential drop so that only two of the four adjacent mesh nodes form filaments. The model contains a cylindrical electrode placed through the mesh to simulate the needle electrode. The end of the cylinder is flush with the dielectric replicating the physical assembly.

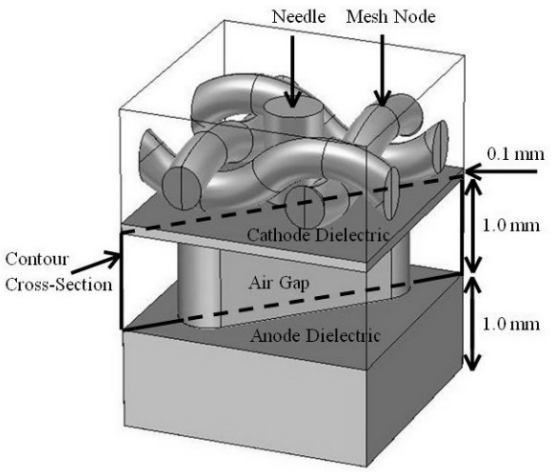

Figure 6. Isometric view of the 3D CST model. The oval volume in the "air gap" defines a section of refined simulation mesh where the filaments form. The remaining air gap volume is not shown for clarity. The "contour cross-section" defines the plane over which the fields are analyzed.

The potential boundary conditions consisted of (1) a zero voltage applied to the mesh (cathode electrode), (2) the maximum driving voltage applied to the external surface of the 1.0 mm dielectric (anode electrode), and (3) the measured needle voltage applied to the cylindrical needle electrode. The boundary conditions perpendicular to the dielectric surface allowed only tangential electric fields. Behind the needle and mesh was an open boundary, located 0.5 mm away from the solid model. The materials chosen for the simulation came from the CST library: the dielectrics were lossy glass pyrex ($\varepsilon = 4.87$), the discharge gas gap was air ($\varepsilon = 1.00059$), and the conducting needle and mesh were perfect electrical conductors.

The voltage boundary conditions in the simulation correspond to the maximum measured value of the driving anode voltage and biased needle voltage. Specifically, simulations were completed for maximum driving voltages applied to the anode electrode of 6.5 and 7.5 kV. The 9.0 kV case was not simulated. The needle voltages were 9, 96, 207, 368, and 476 V for the 6.5 kV case and

10, 115, 230, 435, and 555 for the 7.5 kV case, corresponding with the resistive biases of 0.2, 2, 5, 10, and 15 MΩ, respectively. Results for the 6.5 and 7.5 kV cases show identical trends, with changes in the electric field directly proportional to the change in voltage. Therefore, only the 6.5 kV results are reported below. Since the magnitudes of the fields change proportionally with the driving voltage, a trend and analysis can still be performed to find the relevant field characteristics that affect the variation of the needle plasma filament light intensity.

4.0 RESULTS AND DISCUSSION

4.1 Electrostatic DBD Field Simulation Results

4.1.1 Longitudinal electric field

The contour map of the longitudinal electric field (normal to the dielectric), over the cross-section outlined in Figure 6, is shown in Figure 7. These contour plots display the general form of the electric field for the fully active needle filament (0.2 MΩ) and for no visible evidence of a filament (15 MΩ).

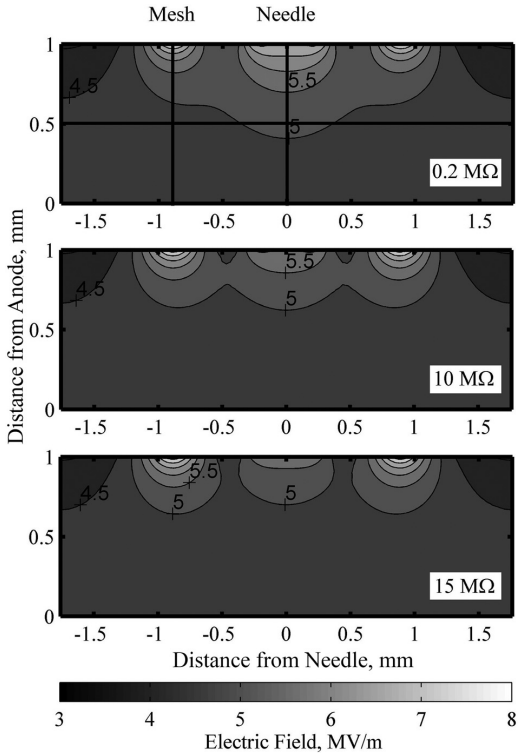

Figure 7. Contour of longitudinal electric field. Three of the five needle bias conditions are presented: 0.2 MΩ, 10 MΩ, and 15 MΩ. The needle filament turn-off occurs between 10 MΩ and 15 MΩ. The vertical lines in the 0.2 MΩ plot define the filament center axes along which the longitudinal fields in Fig. 8 are analyzed. The horizontal lines at 0 mm, 0.5 mm, and 1 mm from the anode (along the vertical axis) define the lines along which the transverse fields in Fig. 10 are analyzed.

The fields along the needle and mesh filament centerlines, defined by the vertical lines in Figure 2, are shown in Figure 3 at 0.2 MΩ and 15 MΩ. The mesh field near the cathode dielectric surface is at least 11% greater than the needle for all conditions due to the geometric difference between the needle and mesh. The curvature of the mesh wire creates a concentration of the electric field on the cathode dielectric surface, compared with the flat surface of the needle. However, the larger contact surface area of the needle maintains the concentration of the field at a further distance from the cathode. At 15 MΩ, the voltage bias offsets the electric field of the needle, lowering the field at the cathode, which reduces the field concentration at a distance (see Figure 8).

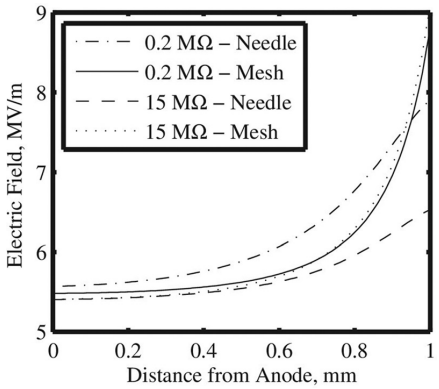

Figure 8. Longitudinal electric field lines at the needle and mesh, for 0.2MΩ and 15MΩ. The longitudinal fields across the air gap show that the needle field is always less than the mesh for the 15 MΩ when the needle filament turns off.

The difference between the needle and mesh fields ($\Delta E(x)_{long} = \Delta E(x)_{long\ needle} - \Delta E(x)_{long\ mesh}$) is shown in Figure 9, to illustrate this transition. All the bias conditions become positive at some position near the anode, except the 15 MΩ condition. They also all approach zero near the anode, with the 15 MΩ condition having a zero difference at the anode. The second derivative of the curve is negative for the 15 MΩ condition and is positive for the other conditions. For the filament turn-off condition (15 MΩ), both the needle and mesh apply the same amount of longitudinal force on a unit of charge at the dielectric anode, but everywhere else the needle applies a lesser cross-gap force than the mesh.

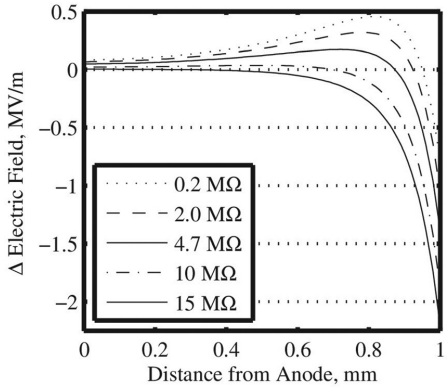

Figure 9. Difference between needle and mesh longitudinal electric fields. The fields are plotted across the air gap from the anode dielectric (z = 0 mm) to the cathode dielectric (z = 1 mm).

4.1.2 Transverse electric field

The transverse field moves free charges toward or away from the filament locations. The transverse fields, along the horizontal lines shown in Figure 7 at 0.0 mm, 0.5 mm, and 1.0 mm from the anode, are plotted in Figure 10 for 0.2 MΩ–15 MΩ conditions. Transverse fields along the anode dielectric (0.0 mm), cathode dielectric (1.0 mm), and at the midplane (0.5 mm) are shown. The vertical lines in Figure 10 correspond to the needle location at 0 mm and the mesh node at – 0.9 mm. Another mesh node is also present at +0.9 mm. These plots illustrate the electric force on a charge between the needle and mesh locations (parallel to the dielectric). It is clear that the transverse fields are strongest at the cathode dielectric, and decrease as one moves toward the anode. This is expected because the anode is biased uniformly (minimal transverse variation in potential), while the cathode has the mesh and needle electrodes which are biased differently (giving rise to strong transverse variation in potential). On the cathode dielectric, the transverse field between the needle and mesh has two peaks, one positive and one negative. The positive peak (near the needle) is the smallest at 15 MΩ due to the decreased voltage difference between the needle and the anode. The negative peak (near the mesh) increases in magnitude (becoming more negative) as needle resistance increases because the corresponding increase in needle voltage creates a stronger potential gradient along the transverse axis. Without the presence of the anode potential, the transverse electric field would purely be directed from the needle towards the mesh with the largest value at 15 MΩ. But due to the presence of the high voltage anode, a transverse potential gradient forms (due to the needle and anode potential difference) creating transverse field directed towards the needle.

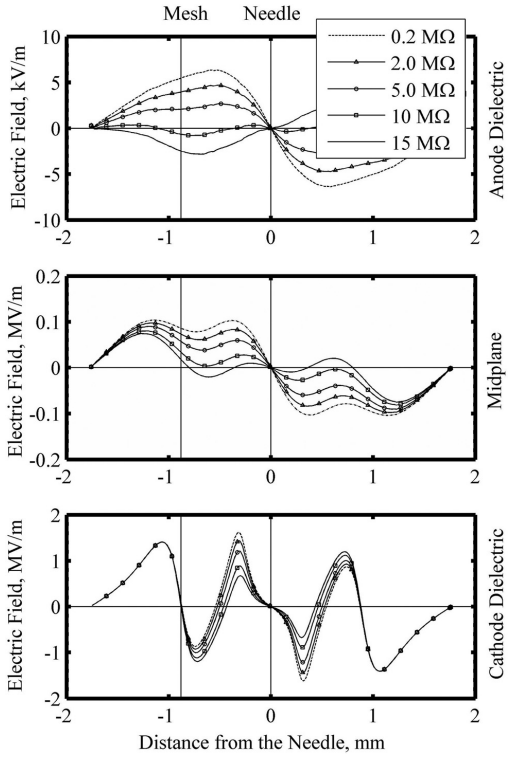

Figure 10. Transverse electric field as a function of transverse position. The lines that define the transverse positions are parallel to the dielectric surface and intersect both mesh and needle filament locations, as shown in Fig. 7. The three figures represent different cross-sectional planes across the air gap (cathode dielectric surface, midplane across the air gap, and the anode dielectric surface).

At the anode dielectric, we see an interesting trend at the needle location. For 0.2 MΩ–10 MΩ, the transverse electric field profile has a negative slope that crosses zero at the needle location, but switches to a positive slope for the 15 MΩ condition (when the needle filament turns off). A negative slope prevents charge from building up at the needle location because an electron to the left (right) of the needle will experience a force to the left (right), moving charge away from the needle location, preserving the longitudinal field, and enabling the filament to form. However, for the 15 MΩ case, the transverse field profile switches to a positive slope crossing zero and the opposite effect occurs. An electron to the left (right) of the needle will experience a force to the right (left), causing electrons to build-up at the needle location, reducing the applied field, and preventing a filament from forming.

4.1.3. Free surface charge limitation

The charge density [C/m^2] on the dielectric surfaces can be estimated with the displacement field from the simulation. The displacement field and a simplified form of Gauss's law[49] (Equation (8)) were used to compare the dielectric surface charge density at the needle with the surface charge density at the mesh. At the interface of the two mediums (dielectric and air), only the normal component of the displacement field affects the surface charge. The difference between the normal components of the displacement field of the dielectric (D_d) and air (D_{air}) equals the surface charge density (σ). The surface charge density builds up on the dielectric during discharge until it reduces the electric field across the gas gap to below the dielectric strength of air (E_b = 3 MV/m), extinguishing the filament. The simulation data are used in the surface integral of Equation (8) to determine the total surface charge at the needle and mesh locations on both the cathode and anode dielectric. The results at the cathode dielectric are plotted as the ratio of the needle surface charge to the mesh surface charge, and are shown in Figure 3 (right y-axis). These results are insensitive (vary < 5%) to the minimum field value used to define the mesh and needle surface areas over which the integral is computed, as long as the integration area does not eliminate or combine the needle and mesh areas. Results from the anode dielectric showed that the surface charge ratio is 1 ± 1% for the 0.2 MΩ condition and 1 ± 0.01% for the 15 MΩ condition. This is to be expected since the longitudinal electric field is uniform across the anode dielectric for all needle bias cases as shown in Figure 7.

$$D_d - \varepsilon_o \varepsilon_{air} E_{air} = \sigma \tag{8}$$

Figure 3 shows that the surface charge ratio at the cathode dielectric is a function of the needle bias resistance. This is to be expected since the longitudinal field at the cathode dielectric changes appreciably as the needle bias resistance is changed, as shown in Figure 7. As needle bias resistance decreases the surface charge ratio increases. At the filament turn-off condition (15 MΩ), the surface charge at the needle and mesh is equal.

4.1.4 Light intensity relationship

Total surface charge, as described in Section 4.1.3, can be related to the expected light emission or light intensity from the plasma filaments. Here, we develop a control volume analysis of the process whereby surface charge is transferred between the dielectrics along a forming plasma filament, and relate the resulting current density to the light emission from the filament. We assume

a static (no time dependence) 1-D model of the early time (first ~20 ns) when the filament is forming. This is the time period over which the majority of the current and light emission occurs, and the density of electrons remains constant.[42] Further, over this short time (much shorter than the AC DBD waveform), the gap voltage is approximately constant and equal to the full applied potential, i.e., the same conditions modeled in our aforementioned simulations. Through this analysis, we relate the ratio of the light emission between the needle and mesh filaments to the ratio of the total surface charge at those locations. The analysis developed here is similar to previous models for streamer and filament formation in air.[42–44]

Consider a control volume that fully contains the plasma filament across the gas gap but does not envelope any adjacent filaments or the radially expanding surface charge. This volume is justified by the thin cylindrical form of the filament and the fact that filaments are spaced at a distance much larger than (about eight times) their diameter. Charge enters through the end of the control volume normal with the dielectric surface. All of the charge supplied to a filament from the dielectric moves along the filament to the opposite dielectric surface, parallel to the surrounding boundaries of the control volume. Electrons are the main charge carrier and their number density and drift velocity traversing the filament are given by the electron current density ($en_e u_e = J_e$). These electrons have ionization collisions with the background gas as they traverse the gap. It is assumed that the emitted light intensity at any position ($\Psi(x,t)$, where x is location along the filament) is proportional to the ionization activity and can be written as the product of the Townsend coefficient (α), electron number density (n_e), and electron drift velocity (u_e) as shown in Equation (9).[42–44] This approach has been successful at describing filament formation and propagation in air.[42–44] If the light of the discharge is recorded along the axis of the filament, and over a time period (in our experiment 125 ms) far greater than the time period over which light emission occurs (~20 ns),[42] then the total measured light intensity (Ψ, per unit area) is the time and length integral of the filament, as shown in Equation (9)

$$\frac{\Psi_{needle}}{\Psi_{\text{mesh}}} = \frac{\iint_{x,t} \Psi(\text{x},\text{t})_{needle} dxdt}{\iint_{x,t} \Psi(\text{x},\text{t})_{needle} dxdt} \propto \frac{\iint_{x,t} [\alpha(x,t) u_e(x,t) n_e(x,t)]_{needle} dxdt}{\iint_{x,t} [\alpha(x,t) u_e(x,t) n_e(x,t)]_{mesh} dxdt} \tag{9}$$

The density of electrons remains constant during the major charge transfer period over the first ~20 ns,[42] when the majority of the current and light emission occurs.[42] By charge conservation ($\nabla \cdot J_e = 0$; $J_{e,r} = J_{e,\theta} = 0$; $J_{e,x} \neq 0$), the current density along the length of the control volume is constant. Therefore, the space-time integral of the current density over the period of the filament discharge and the length of the plasma filament (L) yields the charge density (σ), as shown in Equation (10). The constant cross-sectional area of the control volume (A) and constant charge density due to charge conservation mean that the total charge is constant along the length of the filament. The resulting expression, in Equation (10), relates the length and cross-sectional area of the filament, and the total charge (Q), to the space-time integral of the current density. This relationship shows that all the charge (Q) is transferred from the dielectric surface across the gap through the filament. This relationship enables Equation (9) to be recast as Equation (11)

$$\iint_{x,t} u_e n_e dxdt = \iint_{x,t} J_e dxdt = \sigma L = \frac{QL}{A} \tag{10}$$

$$\frac{\Psi_{needle}}{\Psi_{\text{mesh}}} = \frac{\iint_{x,t} \Psi(\text{x},\text{t})_{needle} dxdt}{\iint_{x,t} \Psi(\text{x},\text{t})_{needle} dxdt} \propto \frac{\left(\frac{QL}{A}\right)_{needle} \iint_{x,t} [\alpha(x,t)]_{needle} dxdt}{\left(\frac{QL}{A}\right)_{mesh} \iint_{x,t} [\alpha(x,t)]_{mesh} dxdt} \tag{11}$$

The Townsend coefficient (α) is given as Equation (12) and is dependent on the pressure and electric field in the gap. In this model, the Townsend coefficient is constant with respect to time because the simulated field values (Efield) and pressure are constant on the filament formation timescale. The pressure is 1 atm, and a collection of literature data from a Sandia National Laboratories Report[50] appropriate to these experimental conditions provides the curve-fits for the coefficients A = 8.805 and B = 258.45. The first Townsend coefficient is integrated over the length of the filament, using Equation (12). However, due to the small variation between the electric field at the needle and mesh locations, the ratio of the integrated Townsend coefficient at the needle and mesh locations is 1 ± 0.002 for all voltage bias conditions. Finally, both the needle and mesh filament control volume have the same length (L) and are assigned the same area (A) so that the resulting light intensity ratio (Eq. (11)) is directly proportional to the ratio of total surface charge (Q), as shown in Equation (13)

$$\alpha(x) = pAexp\left(\frac{-Bp}{E}\right) \tag{12}$$

$$\frac{\Psi_{needle}}{\Psi_{\text{mesh}}} \propto \frac{(Q)_{needle}}{(Q)_{mesh}} \tag{13}$$

A comparison of experimentally measured filament light intensity ratio $\frac{\Psi_{needle}}{\Psi_{mesh}}$ with simulation results of the total surface charge ratio $\frac{(Q)_{needle}}{(Q)_{mesh}}$ is shown in Figure 3. Equation (13) suggests that the ratio of filament light intensity between the needle and mesh locations should be proportional to the total surface charge ratio between those locations. Figure 3 indeed shows this relationship. As Figure 3 shows, the calculated surface charge ratio falls along the measured intensity ratio for 6.5 kV, 7.5 kV, and 9.0 kV driving voltages, albeit with an offset of 1. That is, the surface charge ratio values are offset by the surface charge at the mesh location. This unity offset can be justified when one considers there will be a condition where charge exists at the surface of the dielectric but not enough to initiate a discharge. That condition appears to be the case when the charge ratio between mesh and needle position is 1:1. Figure 3 also shows that the surface charge at the needle must be double that at the mesh (surface charge ratio of 2) when the needle light intensity is equal to that at the mesh (light intensity ratio of 1). Accounting for this unity offset, the calculated surface charge ratio is then within 4%, 11%, 12%, 26%, and 5% of the average

measured light intensity ratio for bias values of 0.2, 2, 5, 10, and 15 MΩ, respectively. At 10 MΩ for 7.5 kV, the measured ratio is 160% larger than the calculated surface charge ratio. This trend may be due to additional surface charge built up across the dielectric surface, over areas of the mesh wire not in contact with the dielectric. Additional charge would allow for continued discharge at the filament before the turn-off condition. The agreement of calculated and measured data suggests that the trend of light intensity can be correlated with the transferred charge when adjusted for the turn-off condition.

4.2 DISCUSSION OF EXPERIMENTAL RESULTS

The mechanism which varies the light intensity is dependent on the charge distribution within the discharge gap rather than the total voltage drop across the gap. This is supported by the characteristics of the turn-off condition: (1) The minimum cross-gap voltage difference of one driving voltage condition does not drop below the maximum cross-gap voltage of a lower condition. (2) None of the conditions drop below the breakdown voltage of air (~3 MV m^{-1}).[2] (3) The turn-off voltage remains at 7% of the driving voltage for all three conditions representing a proportional distribution rather than a total field value. (4) The current drop necessary for filament turn-off at the needle is the same for each driving voltage condition while the total current increases with the driving voltage. This indicates a relative charge buildup rather than a total charge build up. Redistribution of charge over the dielectric surfaces or within the discharge gap displaces the field or limits the filament forming charge.

The movement of charge within the DBD due to the applied electric field displaces the filament-forming longitudinal field, and controls the formation and intensity of the needle filament. Cross-gap charge motion is dominated and controlled by the longitudinal field. The transverse electric field is less than 16% of the longitudinal field. Since the distance between the dielectrics (1.0 mm) is on the order of the distance between the needle and mesh position (0.88 mm), free charge movement between the dielectrics is dominated by longitudinal motion, and the transverse field does not significantly affect the charge distribution during the discharge period. The majority of transverse charge movement will then occur on the charged dielectric surfaces, where the longitudinal force is balanced by the normal force against the dielectric.

The transverse fields affect surface charges over microseconds of the driving voltage rise time, rather than nanoseconds of the discharge period. The transverse fields on the cathode dielectric isolate the needle and mesh charges. However, the transverse electric field on the anode dielectric surface transitions from positive to negative at the 15 MΩ condition, reversing the current direction of surface charge. Charge transfer between the two filaments can appreciably occur only on the anode dielectric surface, which is the dielectric furthest from the needle electrode.

For the reversed driving voltage polarity, the electric field direction reverses on the anode surface. Surface electrons move away from the needle towards the mesh to transfer across the gas gap through the adjacent mesh filaments. The charge movement still displaces the longitudinal field, by matching the lack of charge at the needle, and preventing discharge across the gap.

The variation of the light intensity demonstrates that both permittivity and presence of a filament can be controlled by a voltage bias at a locally selected electrode. The necessary voltage bias for filament turn-off is proportional to the driving voltage, at 7% for this setup.

The bias voltage is an order of magnitude less than the necessary reduction to bring the cross-gap voltage below the breakdown voltage. The simulations demonstrate that the on-off state of a filament can be caused by the difference between the electric fields of two adjacent low voltage electrodes placed behind a dielectric in a DBD. The voltage bias offsets the electric field profile of the needle, lowering the electric field profile of the needle below that of the mesh. Since the discharge control is dependent on the proportionality and not a set voltage limit, further reduction of the controlling voltage value should be possible. These fields are a direct result of the electrode geometries. It is expected that by creating an array of electrodes that are geometrically similar to one another, the voltage bias difference required for filament turn-off can be further reduced from the 476 V, 560 V, and 626 V for the driving voltages of 6.5 kV, 7.5 kV, and 9.0 kV. This voltage reduction mechanism provides a more manageable method for electrically controlling an individual filament. Reducing the necessary voltage difference would make a control circuit for an array of needle filaments a viable option for direct control of individual filament positions and permittivity. The consistency of the light intensity variation between driving voltage conditions suggests that the permittivity of the entire array of filaments may be increased through the driving voltage while maintaining the relative permittivity difference or on-off conditions between filament positions.

4.3 PLASMA PHOTONIC CRYSTAL SIMULATIONS

A plane wave method based off the technique developed by Zhang, et. al.[33] was implemented to make experimental predictions, form estimates of the operational frequency range, determine the necessity for continuous plasma position control, and determine optimal design conditions for a variable plasma photonic crystal prototype. The technique is an adaptation of the plane wave method developed by Kuzmiak and Maradudin[51] which is a linearized eigenvalue problem that incorporates the non-linear frequency dependent plasma dielectric which is defined by the plasma frequency. The adaptation by Zhang discretizes the area covered by the unit cell into a grid of background dielectric or plasma. The method was chosen as a general prediction that is independent of the number of crystal structure unit cells since it assumes a Floquet boundary condition where the cells are repeated infinitely. It produced a relatively generic approach for trend analysis of the bandgaps for different photonic crystal parameters over the obtainable range of a plasma filament photonic crystal. The grid method of the dielectric distribution allowed for modification to model different plasma densities throughout the unit cell and will be used to represent tuning the electron density of adjacent filaments. The method can also form generic geometric structures so that a variety of lattice structures and incident orientations can be analyzed when forming experimental predictions. The method is simple enough to implement so that it can be fully manipulated for parameterization.

4.3.1 Plane wave method derivation

The plane wave method is an approach that uses a mathematical summation of plane waves to define a more complex propagating electromagnetic wave. The derivation of this method will be to use an expression that defines the crystal structure, apply it to Maxwells equations, and rearrange the function so that it can be expressed as a linear eigenvalue problem which is numerically solvable. The eigen value problem is formed from the Helmholtz equations[2] – a frequency domain expression of the Maxwell's equations.

$$\nabla \times H(\boldsymbol{x}, \omega) = i\omega\varepsilon_o\varepsilon_{eff}(\omega)E(\boldsymbol{x}, \omega) \tag{14}$$

$$\nabla \times E(\boldsymbol{x}, \omega) = -i\omega\mu_o H(\boldsymbol{x}, \omega) \tag{15}$$

The position vector ($\boldsymbol{x}$) and the frequency (ω) fully define the electric (E) and magnetic (H) fields. For plasma the permeability (μ_o) is the same as free space but the plasma permittivity (ε_{eff}) due to the free charges is defined by Equation (1). The Equation (14) and Equation (15)are used to derive equations independent for each field.

$$\nabla \times \big(\nabla \times E(\boldsymbol{x}, \omega)\big) = \left(\frac{\omega}{c}\right)^2 \varepsilon_{eff}(\omega)E(\boldsymbol{x}, \omega) \tag{16}$$

$$\nabla \times \left(\frac{1}{\varepsilon_{eff}(\omega)}\nabla \times H(\boldsymbol{x}, \omega)\right) = -\left(\frac{\omega}{c}\right)^2 H(\boldsymbol{x}, \omega) \tag{17}$$

The waves are assumed to be transverse electric (TE) and transvers magnetic (TM) with the transverse component perpendicular to the repeated 2D (two dimensional) lattice structure. Continuing with just the electric field as an example, the Bloch plane wave, Equation (18), and the frequency space representation of the permittivity, Equation (19), are substituted into Equation (16) to produce Equation (20).

$$\boldsymbol{E}(x, w) = \sum_G A(\boldsymbol{k}, \boldsymbol{G_m})e^{i(\boldsymbol{k}+\boldsymbol{G_m})*\boldsymbol{x}} \tag{18}$$

$$\varepsilon(x, w) = \sum_{\boldsymbol{G_n}} \hat{\varepsilon}(\boldsymbol{G_n})e^{i(\boldsymbol{G_n})*\boldsymbol{x}} \tag{19}$$

$$\nabla \times \left(\nabla \times \sum_{G_m} A(\boldsymbol{k}, \boldsymbol{G_m})e^{i(\boldsymbol{k}+G_m)*\boldsymbol{x}}\right) = \left(\frac{\omega}{c}\right)^2 \sum_{\boldsymbol{G_n}} \hat{\varepsilon}(\boldsymbol{G_n})e^{i(\boldsymbol{G_n})*\boldsymbol{x}} \sum_G A(\boldsymbol{k}, \boldsymbol{G_m})e^{i(\boldsymbol{k}+\boldsymbol{G_m})*\boldsymbol{x}} \tag{20}$$

The summation constants A are any values that will solves the equation. The wave vector (k) is the direction and wavelength of the plane wave in phase space and the reciprocal lattice vector (G) is a series of periodic locations in phase space representing the repetition of the lattice $G_x = \frac{2\pi n}{a}$, $G_y = \frac{2\pi n}{a}$. The G_m and the G_n are to differentiate between the sum of permittivity and that of the electric field. For clarity Figure 11 shows examples of different locations identified by the reciprocal lattice vector.

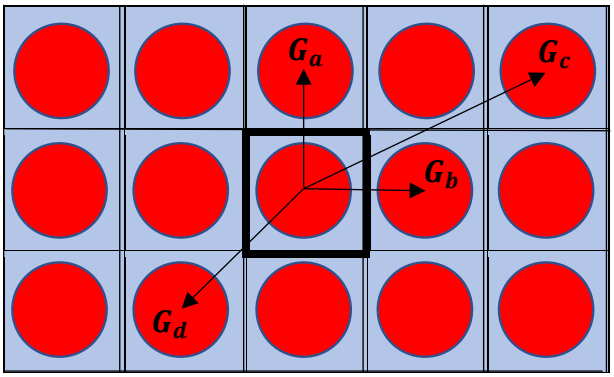

Figure 11. Visual representation of the reciprocal lattice vector (G) in a lattice structure phase space. The dark box is the initial unit cell of the lattice and the surrounding cells are mathematically represented by the reciprocal lattice vector.

The curls of the left of Equation (20) are applied and produce Equation (21). For this case the E-field is in the z-direction, so the other vectors are only in the x-y plane.

$$\sum_{G_m} (\boldsymbol{k} + \boldsymbol{G_m})^2 A(\boldsymbol{k}, \boldsymbol{G_m}) e^{i(\boldsymbol{k}+G_m)*\boldsymbol{x}} \tag{21}$$

$$= \left(\frac{\omega}{c}\right)^2 \sum_{\boldsymbol{G_n}} \hat{\varepsilon}(\boldsymbol{G_n}) e^{i(\boldsymbol{G})*\boldsymbol{x}} \sum_{G_m} A(\boldsymbol{k}, \boldsymbol{G_m}) e^{i(\boldsymbol{k}+G_m)*\boldsymbol{x}}$$

The following summation identity is used to simplify the expression.

$$\sum_{n=1} a_n x_n \sum_{m=1} b_m y_m = \sum_{n=1} \sum_{m=1} a_n x_n b_m y_m \tag{22}$$

$$\sum_{G_m} (\boldsymbol{k} + \boldsymbol{G})^2 A(\boldsymbol{k}, \boldsymbol{G}_m) e^{i(\boldsymbol{k}+\boldsymbol{G_m})*\boldsymbol{x}} \tag{23}$$

$$= \left(\frac{\omega}{c}\right)^2 \sum_{G_m} \sum_{G_n} \hat{\varepsilon}(\boldsymbol{G_n}) e^{i(\boldsymbol{G_n})*\boldsymbol{x}} A(\boldsymbol{k}, \boldsymbol{G_m}) e^{i(\boldsymbol{k}+\boldsymbol{G_m})*\boldsymbol{x}}$$

Although G_m is located on the left and right side of Equation (22), a different series is included for clarity (G_l) which has the same values as G_m but in an arbitrarily different order. Substituting $G_n = G_l - G_m$, the exponential term on the right and left side of the expression become identical.

$$\sum_{G_l} (\boldsymbol{k}+\boldsymbol{G_l})^2 A(\boldsymbol{k},\boldsymbol{G_l}) e^{i(\boldsymbol{k}+\boldsymbol{G_l})*\boldsymbol{x}} \tag{24}$$

$$= \left(\frac{\omega}{c}\right)^2 \sum_{G_m} \sum_{\boldsymbol{G_l}-\boldsymbol{G_m}} \hat{\varepsilon}(\boldsymbol{G_l}-\boldsymbol{G_m}) A(\boldsymbol{k},\boldsymbol{G_m}) e^{i(\boldsymbol{k}+\boldsymbol{G_l})*\boldsymbol{x}}$$

At this point it is helpful to include an example of the matrix equation to visualize the problem.

$$\begin{bmatrix} (\boldsymbol{k}+\boldsymbol{G}_{l=1})^2 & 0 & 0 \\ 0 & (\boldsymbol{k}+\boldsymbol{G}_{l=2})^2 & 0 \\ 0 & 0 & (\boldsymbol{k}+\boldsymbol{G}_{l=3})^2 \end{bmatrix} \begin{bmatrix} e^{i(\boldsymbol{k}+\boldsymbol{G}_{l=1})*\boldsymbol{x}} & 0 & 0 \\ 0 & e^{i(\boldsymbol{k}+\boldsymbol{G}_{l=2})*\boldsymbol{x}} & 0 \\ 0 & 0 & e^{i(\boldsymbol{k}+\boldsymbol{G}_{l=3})*\boldsymbol{x}} \end{bmatrix} \begin{bmatrix} A(\boldsymbol{G}_{l=1}) \\ A(\boldsymbol{G}_{l=2}) \\ A(\boldsymbol{G}_{l=3}) \end{bmatrix} = \tag{25}$$
$$\left(\frac{\omega}{c}\right)^2 \begin{bmatrix} \hat{\varepsilon}(\boldsymbol{G}_{l=1}-\boldsymbol{G}_{m=1}) & \hat{\varepsilon}(\boldsymbol{G}_{l=1}-\boldsymbol{G}_{m=2}) & \hat{\varepsilon}(\boldsymbol{G}_{l=1}-\boldsymbol{G}_{m=3}) \\ \hat{\varepsilon}(\boldsymbol{G}_{l=2}-\boldsymbol{G}_{m=1}) & \hat{\varepsilon}(\boldsymbol{G}_{l=2}-\boldsymbol{G}_{m=2}) & \hat{\varepsilon}(\boldsymbol{G}_{l=2}-\boldsymbol{G}_{m=3}) \\ \hat{\varepsilon}(\boldsymbol{G}_{l=3}-\boldsymbol{G}_{m=1}) & \hat{\varepsilon}(\boldsymbol{G}_{l=3}-\boldsymbol{G}_{m=2}) & \hat{\varepsilon}(\boldsymbol{G}_{l=3}-\boldsymbol{G}_{m=3}) \end{bmatrix} \begin{bmatrix} e^{i(\boldsymbol{k}+\boldsymbol{G}_{l=1})*\boldsymbol{x}} & 0 & 0 \\ 0 & e^{i(\boldsymbol{k}+\boldsymbol{G}_{l=2})*\boldsymbol{x}} & 0 \\ 0 & 0 & e^{i(\boldsymbol{k}+\boldsymbol{G}_{l=3})*\boldsymbol{x}} \end{bmatrix} \begin{bmatrix} A(\boldsymbol{G}_{m=1}) \\ A(\boldsymbol{G}_{m=2}) \\ A(\boldsymbol{G}_{m=3}) \end{bmatrix}$$

Since the series G_m and G_l have the same integer values, they can be arranged in the matrix with the series along the row matching the integer order along the column so that both sides of the matrix have the same exponent and summation constants. By this method, the exponential diagonal matrix can be cancelled leaving

$$\begin{bmatrix} (\boldsymbol{k}+\boldsymbol{G_1})^2 & 0 & 0 \\ 0 & (\boldsymbol{k}+\boldsymbol{G_2})^2 & 0 \\ 0 & 0 & (\boldsymbol{k}+\boldsymbol{G_3})^2 \end{bmatrix} \begin{bmatrix} A(\boldsymbol{G_{l=1}}) \\ A(\boldsymbol{G_{l=2}}) \\ A(\boldsymbol{G_{l=3}}) \end{bmatrix} - \tag{26}$$
$$\left(\frac{\omega}{c}\right)^2 \begin{bmatrix} \hat{\varepsilon}(\boldsymbol{G}_{l=1}-\boldsymbol{G}_{m=1}) & \hat{\varepsilon}(\boldsymbol{G}_{l=1}-\boldsymbol{G}_{m=2}) & \hat{\varepsilon}(\boldsymbol{G}_{l=1}-\boldsymbol{G}_{m=3}) \\ \hat{\varepsilon}(\boldsymbol{G}_{l=2}-\boldsymbol{G}_{m=1}) & \hat{\varepsilon}(\boldsymbol{G}_{l=2}-\boldsymbol{G}_{m=2}) & \hat{\varepsilon}(\boldsymbol{G}_{l=2}-\boldsymbol{G}_{m=3}) \\ \hat{\varepsilon}(\boldsymbol{G}_{l=3}-\boldsymbol{G}_{m=1}) & \hat{\varepsilon}(\boldsymbol{G}_{l=3}-\boldsymbol{G}_{m=2}) & \hat{\varepsilon}(\boldsymbol{G}_{l=3}-\boldsymbol{G}_{m=3}) \end{bmatrix} \begin{bmatrix} A(\boldsymbol{G_{m=1}}) \\ A(\boldsymbol{G_{m=2}}) \\ A(\boldsymbol{G_{m=3}}) \end{bmatrix}$$
$$= 0$$

Each row can be expressed as a linear equation

$$\delta_{l=m}(\boldsymbol{k}+\boldsymbol{G_l})^2 A(\boldsymbol{G}_l) - \left(\frac{\omega}{c}\right)^2 \sum_{\boldsymbol{G_m}} \hat{\varepsilon}(\boldsymbol{G_l}-\boldsymbol{G_m})\, A(\boldsymbol{G_m}) = 0 \tag{27}$$

The reciprocal space permittivity is defined in terms of the Fourier Transform for the real space permittivity, where S is the total area.

$$\hat{\varepsilon}(\boldsymbol{G}) = \frac{1}{S} \iint_S \varepsilon(\boldsymbol{x})\, \mathrm{e}^{-\mathrm{i}\mathbf{G}\cdot\mathbf{x}} dS \tag{28}$$

Since permittivity $\varepsilon(\boldsymbol{x})$ is a distributed function dependent upon the position, the permittivity of the unit cell is defined as

$$\varepsilon(\boldsymbol{x}) = \begin{cases} \varepsilon_a & , \textit{in the dielectric} \\ 1 - \dfrac{\omega_{pe}^2}{(\omega^2 - i\omega\nu_c)}, & \textit{in the plasma} \end{cases} \tag{29}$$

To implement $\varepsilon(\boldsymbol{x})$ into $\hat{\varepsilon}(\boldsymbol{G})$, (frequency space) the following Boolean function is used.

$$F(\boldsymbol{x}) = \begin{Bmatrix} 0, & in\ the\ dielectric \\ 1, & in\ the\ plasma \end{Bmatrix} \tag{30}$$

The Fourier transform defines the conversion between $\varepsilon(\boldsymbol{x})$ and $\hat{\varepsilon}(\boldsymbol{G})$

$$\hat{\varepsilon}(\boldsymbol{G}) = \frac{1}{S}\iint_{S}\left(\varepsilon_a + \left(1 - \frac{\omega_{pe}^2}{(\omega^2 - i\omega\nu_c)} - \varepsilon_a\right)F(\boldsymbol{x})\right)\mathrm{e}^{-\mathrm{i}\mathbf{G}\cdot\mathbf{x}}dS \tag{31}$$

Equation (31) is converted to discreet values for computation

$$\hat{\varepsilon}(\boldsymbol{G}) = \frac{1}{S}\sum_{x}\sum_{y}\left(\varepsilon_a + \left(1 - \frac{\omega_{pe}^2}{(\omega^2 - i\omega\nu_c)} - \varepsilon_a\right)F(x,y)\right)\ \mathrm{e}^{-\mathrm{i}\left(\mathrm{G_x}\cdot\mathrm{x}+\mathrm{G_y}\cdot y\right)}\Delta x\Delta y \tag{32}$$

This summation is separated into two terms that are easier to manage, Equation (34) and Equation (35):

$$\hat{\varepsilon}(\boldsymbol{G}) = \theta(G) + \frac{\eta(G)}{\omega^2 - i\omega\nu_c} \tag{33}$$

$$\theta(G) = \frac{1}{S}\sum_{x}\sum_{y}(\varepsilon_a - \varepsilon_a F(x,y) + F(x,y))\ \mathrm{e}^{-\mathrm{i}\left(\mathrm{G_x}\cdot\mathrm{x}+\mathrm{G_y}\cdot y\right)}\Delta x\Delta y \tag{34}$$

$$\eta(G) = \frac{1}{S}\sum_{x}\sum_{y}\left(\omega_{pe}^2 F(x,y)\right)\ \mathrm{e}^{-\mathrm{i}\left(\mathrm{G_x}\cdot\mathrm{x}+\mathrm{G_y}\cdot y\right)}\Delta x\Delta y \tag{35}$$

These values are substituted into Equation (27).

$$-\delta_{l=m}(\boldsymbol{k}+\boldsymbol{G_l})^2 + \delta_l\left(\frac{\omega}{c}\right)^2\sum_{\boldsymbol{G_m}}\theta(G_l - G_m) - \frac{\eta(G_l - G_m)}{(\omega^2 - i\omega\nu_c)} = 0 \tag{36}$$

Then Multiplied on both sides by $\omega^2 - i\omega\nu_c$ to remove the frequency from the denominator.

$$0 = -(\omega^2 - i\omega\nu_c)\delta_{lm}(\boldsymbol{k}+\boldsymbol{G_l})^2 + \left(\frac{\omega}{c}\right)^2((\omega^2 - i\omega\nu_c)\theta - \eta) \tag{37}$$

Redistributing frequency terms and collecting like terms

$$0 = \frac{\omega^4}{c^2}\ \theta - \frac{\omega^3}{c^2} i\nu_c\theta - \ \omega^2\left(\frac{\eta}{c^2} + \delta_{lm}(\boldsymbol{k}+\boldsymbol{G_l})^2\right) + i\omega\nu_c\delta_{lm}(\boldsymbol{k}+\boldsymbol{G_l})^2 \tag{38}$$

Finally multiplying both sides by $\frac{1}{\omega c}$

$$0 = \left(\frac{\omega}{c}\right)^3\theta - \left(\frac{\omega}{c}\right)^2\frac{i\nu_c}{c}\theta - \left(\frac{\omega}{c}\right)\left(\frac{\eta}{c^2} + \delta_{lm}(\boldsymbol{k}+\boldsymbol{G_l})^2\right) + \frac{i\nu_c}{c}\delta_{lm}(\boldsymbol{k}+\boldsymbol{G_l})^2 \tag{39}$$

Each of these terms is a matrix that has the previously described G_m and G_l order associated with them. The linearization process[51] relates Equation (39) as the determinate of a block matrix and then solves that block matrices eigenvalue problem with $\lambda = \left(\frac{\omega}{c}\right)$ as the single unknown. The eigenvalue problem can then be solved numerically. If the eigenvalue problem is

$$Qz - \lambda Vz = 0 \tag{40}$$

And the block matrices are

$$V = \begin{bmatrix} \boldsymbol{I} & 0 & 0 \\ 0 & \boldsymbol{I} & 0 \\ 0 & 0 & \boldsymbol{X}_3 \end{bmatrix} \qquad Q = \begin{bmatrix} 0 & \boldsymbol{I} & 0 \\ 0 & 0 & \boldsymbol{I} \\ \boldsymbol{X}_0 & \boldsymbol{X}_1 & \boldsymbol{X}_2 \end{bmatrix} \tag{41}$$

Then the determinate is expressed as

$$\boldsymbol{X}_3\lambda^3 - \boldsymbol{X}_2\lambda^2 - \boldsymbol{X}_1\lambda - \boldsymbol{X}_0 = 0 \tag{42}$$

And the coefficients from Equation (39) can represent the block matrix as

$$\boldsymbol{X}_3 = \frac{1}{S}\sum_x\sum_y\left(\varepsilon_a\ + (1 - \varepsilon_a)F(x,y)\right)\mathrm{e}^{-\mathrm{i}\left((\mathrm{G_{xl}}-\mathrm{G_{xm}})\cdot x+(\mathrm{G_{yl}}-\mathrm{G_{ym}})\cdot y\right)}\Delta x\Delta y \tag{43}$$

$$\boldsymbol{X}_2 = \frac{i\nu_c}{c}\frac{1}{S}\sum_x\sum_y\left(\varepsilon_a\ + (1 - \varepsilon_a)F(x,y)\right)\mathrm{e}^{-\mathrm{i}\left((\mathrm{G_{xl}}-\mathrm{G_{xm}})\cdot x+(\mathrm{G_{yl}}-\mathrm{G_{ym}})\cdot y\right)}\Delta x\Delta y \tag{44}$$

$$\boldsymbol{X}_1 = \delta_{lm}(\boldsymbol{k}+\boldsymbol{G_l})^2 + \frac{1}{c^2}\frac{1}{S}\sum_x\sum_y\left(\omega_{pe}^2F(x,y)\right)\mathrm{e}^{-\mathrm{i}\left((\mathrm{G_{xl}}-\mathrm{G_{xm}})\cdot x+(\mathrm{G_{yl}}-\mathrm{G_{ym}})\cdot y\right)}\Delta x\Delta y \tag{45}$$

$$\boldsymbol{X}_0 = -\frac{i\nu_c}{c}\delta_{lm}(\boldsymbol{k}+\boldsymbol{G}_l)^2 \tag{46}$$

The solution to the eigenvalue problem returns positive, negative, and near zero normalized frequency (ω/c) values for each wave vector. The positive real value is the correct solution. The returned array of values is then ranked low to high, representing the different modes (lines in Figure 12). Our reconstructed model produces good agreement with the Zhang, et. al[33] as demonstrated in the Figure 12. There is a 1% frequency error and a 4.5% wave vector error due the discrete sampling of the wave vector at integers and the image processing for retrieving the data from the plots in the text. The TM mode also agrees with the original data. To modify this set of equations and allow for different plasma frequencies (ω_{pe}), the F(x,y) function is changed for Equation (45) to $D(x,y) = \omega_{pe}^2$ so that the plasma dielectric effect can be a function of position.

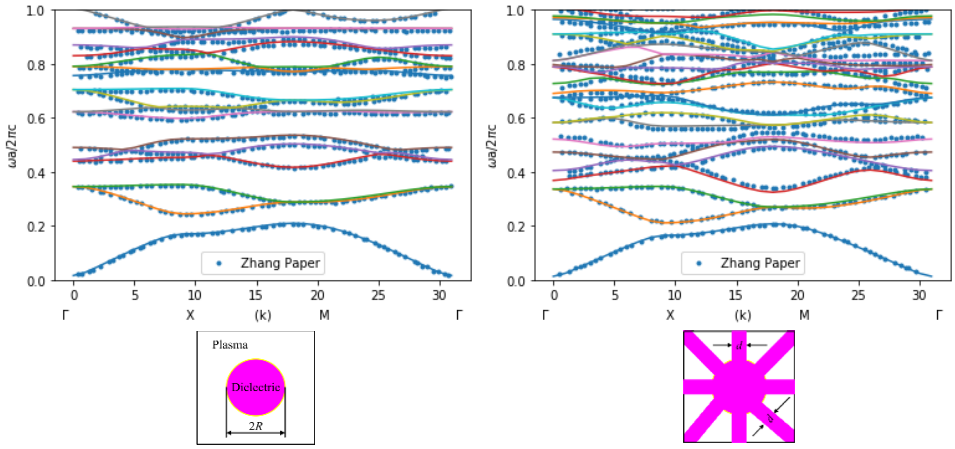

Figure 12. Comparison of the simulation replica with original data for the TE mode (electric field perpendicular to the plane of the unit cell. The replicated simulation (lines) and Zhang's simulations (dots). The diagrams represent the modeled dielectric and plasma distribution of their above bandgaps. (Comparison data and diagrams from Zhang. et. al.[33])

4.3.2 DBD filament parameter trends with TE mode bandgaps

The simulation method was used to produce multiple data points across a range of parameters specific to the DBD plasma photonic crystals. Four parameters were varied: plasma frequency, plasma filament radius, background dielectric, and the lattice constant. The TM and TE modes for these bandgaps were then calculated and catalogued. The collection of bandgaps could then be analyzed for each parameter to determine trends associated with that parameter. The following plots show the resulting trends for the first bandgap in the TE mode and provide insight on further development of a DBD filament photonic crystal. This set of simulations was run with 49 plane waves, a collision frequency that is 2 % of the plasma frequency, and a square lattice constant.

A key question for the design of the DBD filament array is the requirement for position control. For fixed plasma column photonic crystals, the only method for changing the lattice constant is by turning on and off adjacent plasma columns. This doubles the lattice constant at the

lowest lattice constant. This bandgap data shows that the changes due to an integer transition between lattice constants significantly change the available bandgaps. The solid bars across the entire range of lattice constants in the following figures are there to highlight the bandgap frequencies of the integer value bandgaps - 1.0 mm and 2.0 mm. (The solid bars do not represent those bandgaps as being available for all lattice constants).

The effect of the dielectric background, as shown in Figure 13, decreases the average frequency of the bandgap with decreasing background dielectric. The dielectric has no effect on the normalized bandwidth ($\Delta f / f_{avg}$). The highest average frequency of the bandgap is produced by the dielectric of air ($\varepsilon = 1.006$). This is the ideal situation for DBD photonic crystals that operate in gas where the dielectric constant stays near this value regardless of the gas species. Since the dielectric will not change significantly with gas variations, this parameter can be considered fixed in further design processes.

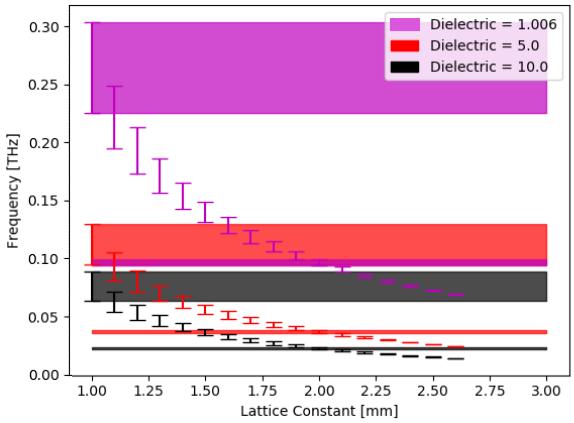

Figure 13. Background dielectric trends with filament radius trends with the frequency bandgap range at each lattice constant. This data is formed with the plasma frequency (ω_{pe} = 0.283 [THz] /n_e = 10^{21} [m^{-3}]) and filament radius (R = 0.4 [mm] fixed. (The solid bands only serve to highlight the bandgaps with multiples of 1.0mm and do not represent a bandgap at all lattice constants for that range of frequencies.)

The trend analyses are aided by examining how the governing equation and dielectric constant relate. By manipulating Equation (16) to isolate the dielectric constant, two parameters in Equation (47) – lattice constant (a) via the del operator ($\nabla \propto 1/a$) and frequency (ω) – govern the proportionality of the dielectric if the electric field is assumed to be a constant. For changes in the dielectric at a fixed lattice constant, the dielectric is proportional to the inverse square of the frequency ($\varepsilon_d \propto 1/\omega^2$). Multiplying the dielectric by the square of the bandgap average frequency ($\varepsilon_d\, \omega^2_{avg}$) and plotting versus the inverse square of the lattice constant ($1/a^2$), Figure 14 shows the consistency of the constant E field assumption.

$$\varepsilon_d = \frac{\nabla \times \nabla \times E(k,G)}{\left(\frac{\omega}{c}\right)^2 E(k,G)} \tag{47}$$

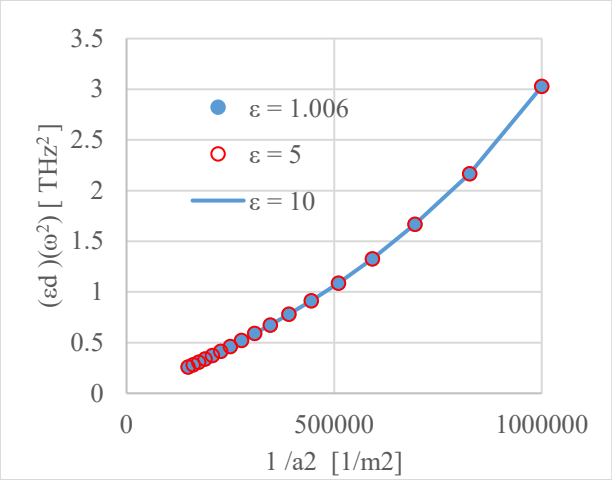

Figure 14. Proportionality of dielectric constant and lattice constant.

All dielectric constants fall along the same line with a slightly linear trend. With the observation that the normalized bandwidth remains constant with changes to the dielectric, it can then be assumed that the normalized bandwidth is proportional to the electric field ratio (∇x∇xE(k,G) / E(k,G)) ratio. The other parameters can now be related to this proportionality to help explain their source of trend data.

Along with the dielectric constant, the lattice constant decreases the bandgap average frequency as shown in Figure 14. However, the normalized bandgap also decreases with increasing lattice constant although Equation (47) suggests otherwise. In this case the impact of the lattice constant as the del operator on the proportionality of the electric fields cannot be ignored. The lattice constant has a more complicated effect on the bandgaps that reduces both the average frequency and bandwidth of the bandgap.

$$\varepsilon\, a^2 = \frac{\Delta\omega}{\left(\frac{\omega_{avg}}{c}\right)^2 \omega_{avg}} \tag{48}$$

Unlike the dielectric trend, the plasma frequency effect on the bandgaps shown in Figure 15 only slightly shifts the average frequency. Instead, the major effect of the plasma frequency is to reduce the bandgap width. The effectiveness of the plasma frequency is exponential as it approaches the average bandgap frequency and disappears as it becomes much less than the plasma frequency.

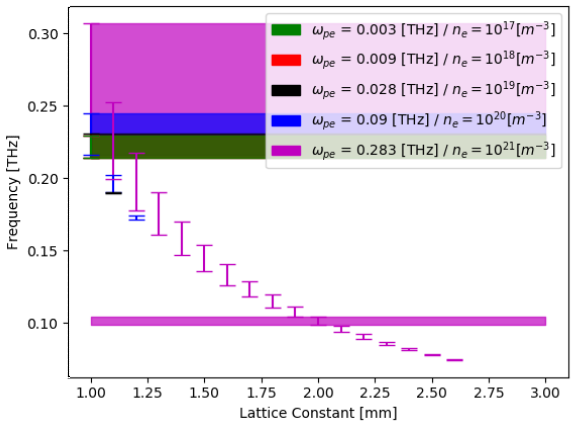

Figure 15. Plasma frequency trends with the frequency bandgap range at each lattice constant. The solid bands only serve to highlight the bandgaps with multiples of 1.0mm and do not represent a bandgap at all lattice constants for that range of frequencies. The dielectric (ε = 1.006) and filament radius (r = 0.4 mm) are fixed.

The expression for the plasma dielectric constant can be analyzed in the same way as the background dielectric. The governing Equation (16) is manipulated into Equation (48) to relate the dielectric constant to the ratio of electric fields. For this dimensional analysis, the collision frequency is ignored since it is a small fraction of the plasma frequency. Then the frequency is redistributed and the resulting Equation (49) shows plasma frequency as an addition term to the electric field that was associated with the normalized bandgap bandwidth from the dielectric trend. If the frequency term (ω) is identified as the average bandgap frequency as was done for the dielectric analysis, then the increase in the bandwidth is due to the addition of the normalized plasma frequency (ω_{pe}). When the plasma frequency is orders of magnitude bellow the average band gap frequency it has little effect since its addition is negligible.

$$\left(1-\frac{\omega_{\mathrm{pe}}^2}{\omega^2-j\omega\nu_c}\right)\left(\frac{\omega}{c}\right)^2=\frac{\nabla\times\nabla\times E(k,G)}{E(k,G)} \tag{49}$$

$$\frac{(\omega^2)}{c^2}=\frac{\nabla\times\nabla\times E(k,G)}{E(k,G)}+\frac{\omega_{\mathrm{pe}}^2}{c^2} \tag{50}$$

The plasma frequency (ω_{pe} = 0.283 [THz (Terahertz)]) with the greatest effect has an equivalent plasma density ($n_e = 10^{21}$ [m^{-3}]) at the upper limit of the atmospheric filament discharge regime. Diffuse or glow plasmas producing electron densities at the lower end of the plotted densities, would have a greatly reduced range of operation even with significant lattice constant control. In this case, strong filament discharges must be formed to produce the desired plasma frequency capability.

The plasma radius affects the bandgaps differently from the previous trends since its relationship to the system is geometric rather than dielectric. The trend in Figure 16 shows a decrease in the normalized bandwidth without significant changes in the average frequency. There is little relative deviation with this trend along the lattice constant. The largest filaments produce the largest bandgaps but bandgaps still exist for low filaments at higher lattice constants.

There is finer control of the bandgaps with the radius diameter over all lattice constants compared with the plasma frequency that almost eliminated bandgaps at all but the lowest lattice constant when the frequency was not at its maximum.

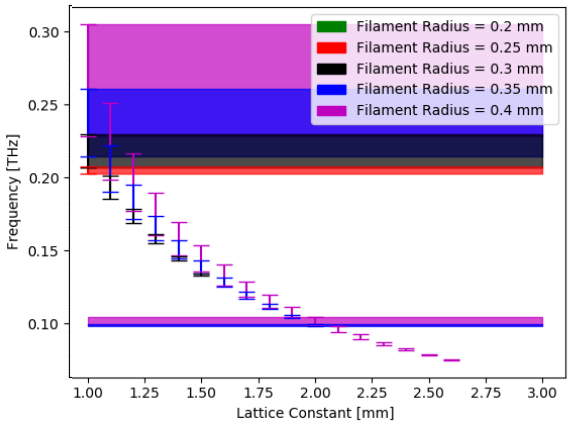

Figure 16. Filament radius trends with the frequency bandgap range at each lattice constant. (The solid bands only serve to highlight the bandgaps with multiples of 1.0mm and do not represent a bandgap at all lattice constants for that range of frequencies.) The plasma frequency (ω_{pe} = 0.283 [THz] /$n_e = 10^{21}$ [m^{-3}]) and dielectric constant (ε = 1.006) are fixed.

Since the radius doesn't have a term in Equation (16), the radius can be related by a filling fraction ($f = \pi R^2/a^2$) to the dielectric.

$$\varepsilon \frac{\pi R^2}{a^2} = \frac{\nabla \times \nabla \times E(k,G)}{\left(\frac{\omega}{c}\right)^2 E(k,G)} \tag{51}$$

Associating the two del operators with the square of the lattice constant ($1/a^2$), the lattice constant on the left can cancel the del operator on the right. Then substituting the electric field ratios for the normalized bandwidth, the area of the filament (πR^2) has a linear relationship with the bandwidth and is independent of the lattice constant.

$$\varepsilon\, \pi R^2 = \frac{\Delta\omega}{\left(\frac{\omega_{avg}}{c}\right)^2 \omega_{avg}} \tag{52}$$

The collection of parameters that effect the band gaps are the lattice constant, plasma frequency, dielectric background, and filament radius. Bandgaps are formed over a range of 5 GHz – 300 GHz at discharge parameters obtainable with DBD filaments. The filament radius and the plasma frequency both control the bandwidth of the bandgap. Increase in either will increase the bandwidth. The lattice constant and the dielectric background both adjust the average bandgap frequency. However, the dielectric does not affect the bandwidth while the lattice constant affects both the average bandgap frequency and bandwidth. Both decrease the frequency values with increasing parameter values.

From these relations and the frequency difference between the 1.0mm and 2.0mm lattice bandgaps, it has been shown that a large portion of frequency space is unobtainable for forming bandgaps without changing the lattice constant or dielectric constant. Since the background gas dielectric is unlikely to significantly change in a DBD discharge, displacing the filament position on scale less than an integer of the smallest lattice is critical. Although another option for achieving this frequency domain could be to affect the dielectric of the background with a reduced plasma frequency discharge at alternating filament locations. The secondary plasma filament would act as background dielectric with reduced effect compared with the primary filament discharge.

5.0 CONCLUSION

The data presented above demonstrate the capability of a non-driving voltage bias applied to an individual electrode to vary the intensity of, and to turn-off, a single filament, while adjacent to other discharging filaments in a DBD. The light intensity of the filament ranges between 100% and 0% of the surrounding filaments' intensities, and is representative of the plasma density. Peak voltages of 476 V and 560 V respective to the 6.5 kV and 7.5 kV driving voltages are required to transition the filament from full-on to full-off; however, lesser voltage changes of 100 V can cause the observed transition between a discharging filament and no filament. This small voltage change, relative to the driving voltage, keeps the voltage difference applied across the gas gap above the breakdown voltage for air. The presence of the needle filament is then dependent on charge distribution caused by voltage differences between low voltage electrodes, rather than the total voltage difference across the gas gap.

Investigation into the applied electric fields within the DBD identified that surface charge interactions between the needle-generated filament and its adjacent filaments cause light intensity. Computer simulation of the geometry and measured boundary conditions show field trends that coincide with the 15 MΩ turn-off condition. The filament turns off when: (1) the applied electric field profile along the needle filament lies below the mesh filament; (2) on the dielectric closest to the needle and mesh electrodes, the charge over both electrodes is equal; and (3) the transverse field on the anode dielectric between the needle and the mesh reverses direction.

These trends are associated with the movement of electrons on the dielectric surface furthest from the needle and mesh electrodes (the anode in the simulation). Along the anode dielectric, electrons transferred from the mesh to the needle position displace the longitudinal field of the needle so that there is no filament formation at 15 MΩ. Effects of charge transfer in the air gap or on the dielectric surface closest to the needle and mesh electrodes (cathode in the simulation) were eliminated as significant transverse charge movement regions, due to inhibiting fields.

The variation of the experimental light intensity was related to the total charge transferred across the filament, and calculated using dielectric surface charge. The calculated light trend was shifted to zero at 15 MΩ, to match the observed lack of discharge. However, the experimental light intensity trend agrees with the calculated surface charge trend to within 8%. A charge decrease equal to the total charge at the mesh filament is the difference between the full light intensity and no light emission at the needle filament.

As an initial step towards constructing a variable plasma photonic crystal with this the physical phenomenon, a plane wave method for modeling plasma photonic crystals was reconstructed from literature and implemented. The simulations produced prediction for an

applicable frequency range [5 – 300 GHz], trends of the controlling parameters, and dependence on lattice constant mobility. The plasma frequency and the filament radius could only control the normalized bandwidth of the bandgap. The lattice constant and background dielectric controlled the average frequency of the bandgap. Control of the average frequency provides the largest range of frequency space for the variable photonic crystal. Changing lattice constants by reducing the number of discharging filaments will omit half the possible bandwidth. Offsetting the plasma dielectric between adjacent filaments to artificially change the background dielectric could provide an alternative to controlling the position of the filament on a scale less than the smallest lattice constant.

Voltage variations that control the presence of a single filament in a PPC are reduced to less than 7% of the independent driving voltage. An explanation has been presented for a lack of plasma discharge where the local peak electric field is above the turn-off dielectric strength of air. Field trends have been presented for identifying filament turn-off points, and making light intensity predictions using an electrostatic field simulation. The controlling voltage bias has been related to the electric field difference between adjacent electrodes, and can be reduced by increasing the geometric similarity of these adjacent electrodes. Bandgap predictions at DBD filament parameters show the possible frequency range of application as between 5 GHz – 300 GHz for the first bandgaps in the TE mode. The developed method of reducing adjacent filaments could provide the ability to produce the bandgaps over this full range of frequencies.

6.0 FOLLOW ON WORK

Future work will consist of experiments to develop and test a variable plasma array (photonic crystal/metamaterial) where the individual filaments can be controlled. Simulations of the microwave field interacting with the plasma filaments will support the testing of this device by making predictions for validation and assisting with designing a plasma array that demonstrates desirable properties – band gaps, all angle negative refraction, and left-handed propagation. The device will be based on the previously presented control method of biasing independent electrodes. This will allow for lattice geometry, lattice constant, plasma frequency, and plasma radius control.

6.1 Variable Plasma Array Construction

Currently a prototype duplicating the previous test geometry (electrode lattice constant, wire electrode diameter, air gap, and dielectric thickness) but with multiple wire electrodes replacing the mesh nodes is being tested. Once the previous results are achieved with this device, multiple biased electrode testing will follow. The will be to change the electron density at alternating filaments or eliminate alternating filaments, effectively changing the lattice constant. Then a digital control mechanism such as a transistor will be integrated to each filament circuit to limit the current and so bias each filament via a computer. The expectation is that the similarity between the electrode geometry would reduce the required voltage bias between the electrodes. The initial difference between the electric field profiles of the mesh and the needle is due to their geometries, where the mesh can be approximated as a point source and the wire electrode as a flat plate. With a reduced initial electric field difference via the same geometries, the biased field difference produced would be more effective and hence require less of a difference for the same effect.

In addition to looking at controlling the filament electron density and radius at each position, we also intend to investigate position control of the filament across the surface of the dielectric. Sinclair and Walhout[29] have shown filaments forming over multiple electrodes at increased breakdown voltages. In this case the filament foot print covered multiple electrodes and the filament itself was positioned at the center of all four electrodes. Since the filament is centered with all electrodes equally biased, it is assumed that the current is also routed evenly through the electrodes. With this assumption a bias between the collection of electrodes located below a single filament would shift the concentration of surface charge, shifting the position of the filament. Position control would then allow for control over the lattice structure (square,[33] hexagonal,[5] and others[34]) and lattice constant at increments bellow the electrode spacing.

6.2 Additional Simulations

Continuation of the plane wave method simulations would include variation of alternate filaments that could be produced by the proposed filament array. The expectation is that the bandgaps at lattice constants between the fixed plasma array integer separation could be formed if the dielectric of the larger lattice constant was partially filled with a reduced plasma dielectric. Transition between these bandgaps could then be obtained at filament separation that are in between the constructed filament array. With the current model this could be simply implemented by adjusting the distribution of the plasma frequency because of its ability to vary the plasma dielectric distribution and implement generic repeatable geometries.

Additional modeling would include finding crystal structure parameters and plane of incident media cut to produce negative refraction for later testing. The negative refraction would be determined by solving for the constant frequency contours of the photonic crystal, satisfying the condition for an in-phase tangential wave vector with the incident medium, determining the transmitted component perpendicular to the constant frequency contour, and finding conditions with a propagation vector in the opposite direction as the incident wave vector. With a program that could find one of these conditions, further processing could determine the necessary photonic crystal parameters and frequency ranges for all-angle negative refraction.

Since the photonic crystal simulation is only appropriate for lattice constant scales where Bragg scattering can contribute to the wave characteristics, modeling the characteristics of the plasma when it operates as a metamaterial – lattice constants far less than the wavelength ($10\ a < \lambda$) – would provide understanding of the plasma arrays potential at lower frequencies. The simulation approach in this case would include simulating the E and H fields formed by excitations over a range of frequencies, averaging the fields as demonstrated by Smith and Pendry52,53 to derive effective parameters. The challenge of plasma metamaterials has been noted by Sakai1 as being their lack of bulk negative permeability. A negative permeability at the resonant permittivity frequency needs to be introduced to form a left-handed propagating wave. A number of approaches demonstrated with thin metal rods53,54 displaying similar plasma dielectric properties could be applied to find a combined negative permeability and permittivity at the same frequency. Simulation to of these methods with the range of possible plasma parameters would determine if this approach is possible in this configuration.

6.3 Microwave Testing

Once the plasma array is constructed, we plan to conduct microwave tests to verify 1) the predicted wave propagation characteristics of the plasma array 2) the variable capabilities of this type of plasma array, and 3) that the structure of this control method does not interfere with the expected wave propagation. The planned approach is to use a pair of horn antennas to direct the microwaves solely through the plasma array, as demonstrated by Sakai, Shimomura, and Tachibana[25] or Matlis, et. al.[55] The transmitted power would be measured with different propagation directions to validate the negative refraction and bandgap predictions of the photonic crystal. For the metamaterial, similar directional tests could be conducted on left handed material to demonstrate their capability. In addition, S-Parameter measurements with conversions to effective parameters[53,56] would provide quantitative measurement of the material permeability and permittivity to compare with the metamaterial predictions.

7.0 BIBILOGRAPHY

[1] O. Sakai and K. Tachibana, Plasma Sources Sci. Technol. **21**, 013001 (2012).

[2] U. Inan, A. Inan, and R. Said, *Engineering Electromagnetics and Waves*, 2nd ed. (Pearson Education Limited, Edinburgh Gate, 2016).

[3] J.B. Pendry, A.J. Holden, W.J. Stewart, and I. Youngs, Phys. Rev. Lett. **76**, 4773 (1996).

[4] J.B. Pendry, A.J. Holden, D.J. Robbins, and W.J. Stewart, IEEE Trans. Microw. Theory Tech. **47**, 2075 (1999).

[5] H.F. Zhang, S. Bin Liu, and B.X. Li, Phys. Plasmas **23**, 012105 (2016).

[6] J. Benford and J. Swegle, *High Power Microwaves* (Artech House, Boston, 1992).

[7] E. Schamiloglu, 2004 IEEE MTT-S Int. Microw. Symp. Dig. **2**, 1001 (2004).

[8] W.M. Manheimer, A.W. Fliflet, K. St. Germain, G.J. Linde, W.J. Cheung, V. Gregers-Hansen, B.G. Danly, and M.T. Ngo, Geophys. Res. Lett. **30**, 5 (2003).

[9] G. V. Marr, *Plasma Spectroscopy* (Elsevier Pub. Co., Amsterdam, 1968).

[10] C.H. Liu, J.D. Neher, J.H. Booske, and N. Behdad, J. Appl. Phys. **116**, 143302 (2014).

[11] R. Seviour, Y.S. Tan, and A. Hopper, 8th Int. Congr. Adv. Electromagn. Mater. Microwaves Opt. 142 (2014).

[12] C.H. Liu, J.D. Neher, J.H. Booske, and N. Behdad, IEEE Trans. Plasma Sci. **42**, 1255 (2014).

[13] M.Y. Naz, A. Ghaffar, N.U. Rehman, S.A. Shahid, and S. Shukrullah, Int. J. Eng. Technol. **12**, 53 (2012).

[14] M.A. (Michael A.. Lieberman and A.J. Lichtenberg, *Principles of Plasma Discharges and Materials Processing* (Wiley-Interscience, Hoboken, 2005).

[15] Y. Itikawa, J. Phys. Chem. Ref. Data **35**, 31 (2006).

[16] H. Ryzko, Proc. Phys. Soc. **85**, 1283 (1965).

[17] B. Eliasson and U. Kogelschatz, IEEE Trans. Plasma Sci. **19**, 1063 (1991).

[18] J. Hartnett, *Advances in Heat Transfer, Volume 40: Transport Phenomena in Plasma*, 1st ed. (Elsevier/Academic Press, 2007).

[19] M. Lim, K.K. Jayapalan, A.Z.S. Zulkifli, H. Hassan, K. Lai, and O. Chin, Int. J. Environ. Sci. Dev. **8**, 50 (2017).

[20] C.H. Kruger, C.O. Laux, L. Yu, D.M. Packan, and L. Pierrot, Pure Appl. Chem. **74**, 337 (2002).

[21] J.H. Kim, Y.H. Choi, and Y.S. Hwang, Phys. Plasmas **13**, 093501 (2006).

[22] U. Kogelschatz, Plasma Chem. Plasma Process. **23**, 1 (2003).

[23] V.I. Gibalov and G.J. Pietsch, Plasma Sources Sci. Technol. **21**, 024010 (2012).

[24] O. Sakai, T. Sakaguchi, and K. Tachibana, J. Appl. Phys. **101**, 073304 (2007).

[25] T. Sakaguchi, O. Sakai, and K. Tachibana, J. Appl. Phys. **101**, 073305 (2007).

[26] O. Sakai, J. Maeda, T. Shimomura, and K. Urabe, Phys. Plasmas **20**, 073506 (2013).

[27] O. Sakai, T. Shimomura, and K. Tachibana, Phys. Plasmas **17**, 123504 (2010).

[28] Y. Wang, L. Dong, W. Liu, Y. He, and Y. Li, Phys. Plasmas **21**, 073505 (2014).

[29] J. Sinclair and M. Walhout, Phys. Rev. Lett. **108**, 035005 (2012).

[30] L. Dong, B. Li, N. Lu, X. Li, and Z. Shen, Phys. Plasmas **19**, 052304 (2012).

[31] W. Fan, X. Zhang, and L. Dong, Phys. Plasmas **17**, 113501 (2010).

[32] L. Dong, J. Shang, Y. He, Z. Bai, L. Liu, and W. Fan, Phys. Rev. E **85**, 066403 (2012).

[33] H.F. Zhang, G.W. Ding, H.M. Li, and S. Bin Liu, Phys. Plasmas **22**, 022105 (2015).

[34] H.F. Zhang, S. Bin Liu, and Y.C. Jiang, Phys. Plasmas **21**, 092104 (2014).

[35] L.B. Loeb and J.M. Meek, J. Appl. Phys. **11**, 459 (1940).

[36] J.M. Meek and J.D. Craggs, *Electrical Breakdown of Gases* (Clarendon Press, Oxford, 1953).
[37] O. Emelyanov and M. Shemet, J. Electrostat. **81**, 71 (2016).
[38] O.A. Emelyanov and M. V. Shemet, J. Phys. D. Appl. Phys. **47**, 315201 (2014).
[39] S. Ma, J. Howard, and N. Thapar, Phys. Plasmas **18**, 083301 (2011).
[40] X. Wang, H. Luo, Z. Liang, T. Mao, and R. Ma, Plasma Sources Sci. Technol. **15**, 845 (2006).
[41] Q. Ye, Y. Wu, X. Li, T. Chen, and G. Shao, Plasma Sources Sci. Technol. **21**, 065008 (2012).
[42] R. Morrow and J.J. Lowke, J. Phys. D. Appl. Phys. **30**, 614 (1997).
[43] A.J. Davies, C.S. Davies, and C.J. Evans, Proc. Inst. Electr. Eng. **118**, 816 (1971).
[44] R. Morrow, Phys. Rev. A **32**, 1799 (1985).
[45] CST of America, (2015).
[46] H.A. Haus and J.R. Melcher, *Electromagnetic Fields and Energy* (Prentice Hall, Englewood Cliffs, NJ, 1989).
[47] D.L. Logan, *A First Course in the Finite Element Method*, 5th ed. (Cengage Learning, Stamford, CT, 2012).
[48] M. Kettlitz, H. Höft, T. Hoder, S. Reuter, K.-D. Weltmann, and R. Brandenburg, J. Phys. D. Appl. Phys. **45**, 245201 (2012).
[49] J.D. Jackson, *Classical Electrodynamics* (Wiley, New York, NY, 1999).
[50] L. Warne, R. Jorgenson, and S. Nicolaysen, *Ionization Coefficient Approach to Modeling Breakdown in Nonuniform Geometries* (Albuquerque, NM, 2003).
[51] V. Kuzmiak and A.A. Maradudin, Phys. Rev. B **55**, 7427 (1997).
[52] D.R. Smith and J.B. Pendry, J. Opt. Soc. Am. B **23**, 391 (2006).
[53] S.A. Ramakrishna and T.M. Grzegorczyk, *Physics and Applications of Negative Refractive Index Materials* (SPIE Press, 2009).
[54] G.V. (George V.. Eleftheriades and K.G. (Keith G.. Balmain, *Negative-Refraction Metamaterials : Fundamental Properties and Applications* (J. Wiley, Hoboken, NJ :, 2005).
[55] E.H. Matlis, T.C. Corke, B. Neiswander, and A.J. Hoffman, J. Appl. Phys. **124**, 093104 (2018).
[56] J.R. Baker-Jarvis, M.D. Janezic, B.F. Riddle, R.T. Johnk, C.L. Holloway, R.G. Geyer, and C.A. Grosvenor, *Measuring the Permittivity and Permeability of Lossy Materials: Solids, Liquids, Metals, and Negative-Index Materials | NIST* (2005).

LIST OF SYMBOLS, ABBREVIATIONS, AND ACRONYMS

1D	One Dimensional
2D	Two Dimensional
3D	Three Dimensional
ABS	Acrylonitrile Butadiene Styrene
AC	Alternating Current
CAD	Computer Aided Design
CST	Computer Simulations Technologies
DBD	Dielectric Barrier Discharge
eV	electron-Volt
GHz	Gigahertz
HPM	High-Power Microwave
kHz	kilohertz
kΩ	kilo ohm
kV	kilovolt
LF	Low Frequency
m	meter
mm	millimeter
MΩ	Mega ohm
ms	millisecond
μs	microsecond
MHz	Megahertz
ns	nanosecond
PPC	Plasma Photonic Crystal
TE	Transverse Electric
THz	Terahertz
TM	Transverse magnetic
V	Volt

DISTRIBUTION LIST

DTIC/OCP
8725 John J. Kingman Rd, Suite 0944
Ft Belvoir, VA 22060-6218 1 cy

AFRL/RVIL
Kirtland AFB, NM 87117-5776 1 cy

Robert Achenbach
Official Record Copy
AFRL/RDHP 1 cy

This page intentionally left blank.